



CrossMark

Estimation of Crust and Lithospheric Properties for Mercury from High-resolution Gravity and Topography

Sander Goossens¹ , Antonio Genova² , Peter B. James³ , and Erwan Mazarico¹ ¹NASA Goddard Space Flight Center, Greenbelt, MD, USA; sander.j.goossens@nasa.gov²Sapienza, University of Rome, Department of Mechanical and Aerospace Engineering, Rome, Italy³Department of Geosciences, Baylor University, Waco, TX, USA

Received 2021 December 16; revised 2022 April 3; accepted 2022 April 28; published 2022 June 23

Abstract

We have analyzed the entire set of radiometric tracking data from the MErcury Surface, Space ENvironment, GEochemistry, and Ranging (MESSENGER) mission. This analysis employed a method where standard Doppler tracking data were transformed into line-of-sight accelerations. These accelerations have greater sensitivity to small-scale features than standard Doppler. We estimated a gravity model expressed in spherical harmonics to degree and order 180 and showed that this model is improved, as it has increased correlations with topography in areas where tracking data were collected when the spacecraft altitude was low. The new model was used in an analysis of the localized admittance between gravity and topography to determine properties of Mercury's lithosphere. Four areas with high correlations between gravity and topography were selected. These areas represent different terrain types: the high-Mg region, the Strindberg crater plus some lobate scarps, heavily cratered terrain, and smooth plains. We employed a Markov Chain Monte Carlo method to estimate crustal density, load density, crustal thickness, elastic thickness, load depth, and a load parameter that describes the ratio between surface and depth loading. We find densities around 2600 kg m^{-3} for three of the areas, with the density for the fourth area, the northern rise, being higher. The elastic thickness is generally low, between 11 and 30 km.

Unified Astronomy Thesaurus concepts: [Mercury \(planet\) \(1024\)](#); [Planetary interior \(1248\)](#); [Planetary structure \(1256\)](#); [Markov chain Monte Carlo \(1889\)](#); [Metropolis-Hastings \(1893\)](#); [Gravitational fields \(667\)](#); [Lithosphere \(928\)](#)

1. Introduction

Knowledge of the planet Mercury's interior structure is important because it can provide constraints on the formation of the solar system, with Mercury being considered an end-member of the formation processes because of both its location close to the Sun and its high average density (e.g., Chapman 1988). The MErcury Surface, Space ENvironment, GEochemistry, and Ranging (MESSENGER) mission was launched in 2004, carrying seven instruments and a radio science investigation to answer questions about Mercury's formation, geological history, magnetic field, core, polar areas, and exosphere (Solomon et al. 2007). MESSENGER provided, among other things, the first view of the entire planet and yielded invaluable data sets. Important for the analysis presented in this work are the first detailed maps of topography (Zuber et al. 2012) and gravity (Smith et al. 2012). A much more complete overview of MESSENGER's accomplishments is given in Johnson & Hauck (2016).

MESSENGER was inserted into a highly elliptical orbit with a period of 12 hr around Mercury on 2011 March 18. After 2012 April, the orbital period was reduced to 8 hr. While its pericenter was initially between 200 and 500 km above the surface of the planet, it was as low as 15–25 km above the surface during the final stages of its second extended mission (which, in its entirety, lasted from 2013 March until 2015 April, the end of the mission). Lower spacecraft altitudes mean better sensitivity with respect to small-scale gravity signals; so,

during the course of the mission, gravity field models were extended in resolution as more low-altitude data became available. The initial gravity field model, called HgM002, was presented in Smith et al. (2012), and it had a resolution of degree and order 20 in spherical harmonics. Using 3 yr of MESSENGER data, Mazarico et al. (2014) presented a model of degree and order 50 called HgM005. Using the same data set, these results were confirmed by the analysis of Verma & Margot (2016), who presented the degree and order 40 model, HgMUCLA40x40. The first model to use the entire set of MESSENGER tracking data was the degree and order 100 model, called HgM008, by Genova et al. (2019). Recently, Konopliv et al. (2020) analyzed the entire MESSENGER data set, increasing the model expansion to degree and order 160, resulting in a series of models called Mess160a.

The Mercury Laser Altimeter (MLA) instrument (Cavanaugh et al. 2007) measured the topography. The most recent models, expressed in spherical harmonics, have a maximum degree and order of 150 (Neumann 2016). Due to the elliptical orbit of MESSENGER and instrument limitations, these models only have sufficient detail in the northern hemisphere. Toward the equator, MLA tracks were much more sparse and can be kilometers away from each other. Topography models based on camera data also exist, both global models (Becker et al. 2016) and those consisting of high-resolution regional quadrangles (Preusker et al. 2018). In our analysis, we use the GTMES150 model based on MLA (Neumann 2016).

A joint analysis of gravity and topography can be used to infer the interior structure of a planet (e.g., Wicczorek 2015). In particular, the transfer function between topography and gravity, called admittance, provides a powerful method to probe the structure of the lithosphere of a planet. An understanding of the



Original content from this work may be used under the terms of the [Creative Commons Attribution 4.0 licence](#). Any further distribution of this work must maintain attribution to the author(s) and the title of the work, journal citation and DOI.

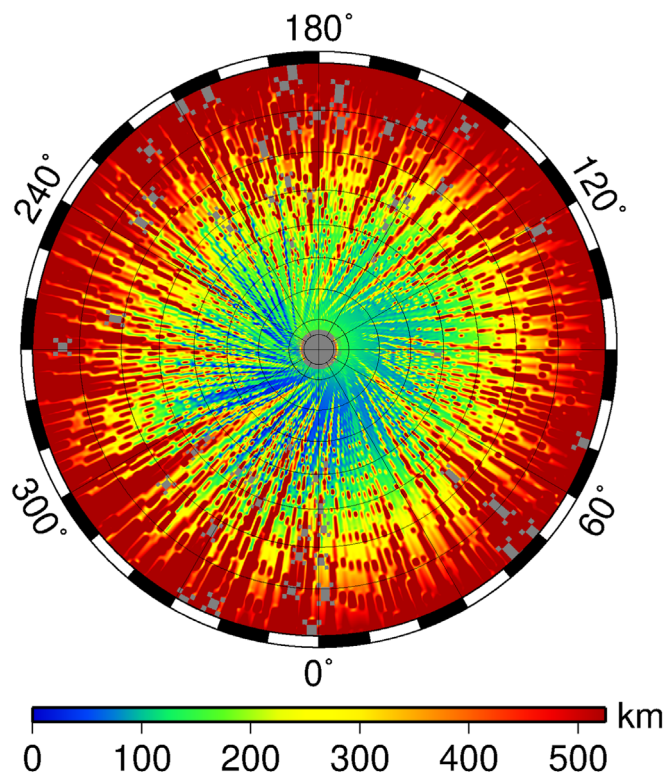


Figure 1. Minimum altitude above Mercury’s surface for MESSENGER tracking data in a north polar stereographic projection down to 10°N.

lithosphere can inform us about Mercury’s interior structure and temperature distribution, and as such, it provides constraints on the history of thermochemical convection (e.g., Solomon 1976; Michel et al. 2013; Tosi et al. 2013), radial contraction (e.g., Hauck et al. 2013; Byrne et al. 2014), and dynamo generation (e.g., Manthilake et al. 2019; Takahashi et al. 2019). Results from the MESSENGER mission have thus been used to study properties such as lithospheric thickness (e.g., Tosi et al. 2015), crustal thickness (e.g., Padovan et al. 2015; Sori 2018; Beuthe et al. 2020a), and topographic support (e.g., James et al. 2015; Kay & Dombard 2019).

Several of these studies relied on earlier gravity field models and were consequently restricted to long-wavelength signals. The short-wavelength part of the gravity field can be used to further probe the properties of the lithosphere, especially the density of the crust. The most recent gravity field models (Genova et al. 2019; Konopliv et al. 2020) contain the low-altitude data and thus have an improved resolution over older models. Yet because of the highly eccentric orbit of MESSENGER, the tracking data coverage shows large spatial variations, as we show in Figure 1. As a result, the gravity field has its best resolution in the northern hemisphere. With increasing degree and order, small-scale features can be described in more detail, but with geographically varying tracking data coverage, the determination of the globally supported spherical harmonics coefficients might become unstable. This determination of a global field then requires regularization, and the choice is often to apply what is called a Kaula rule (Kaula 1966), which biases the coefficients of the spherical harmonic expansion to zero with an expectation that their power is proportional to $1/n^2$, where n is the degree. As a result, the short-wavelength signal is often suppressed (e.g., Konopliv et al. 2001). Regularization methods that take into

account geographically varying data coverage also exist and have been applied at Venus (Konopliv et al. 1999) and Mercury (Konopliv et al. 2020).

Alternative data analysis methods based on local instead of global representations exist, and they have been used successfully in the planetary sciences to determine local gravity fields on the Moon (e.g., Muller & Sjogren 1968; Wong et al. 1971; Goossens et al. 2014), Mars (e.g., Beuthe et al. 2006), Venus (e.g., Barriot & Balmino 1994; Kaula 1996), and Ganymede (Anderson et al. 2004; Palguta et al. 2006). Methods based on line-of-sight (LOS) accelerations (time derivatives of the Doppler tracking data residuals, the difference between measured and modeled tracking data observations) have also been used to determine both local (e.g., Barriot & Balmino 1992) and global (e.g., Barriot et al. 1998) gravity fields. They have also been used to directly determine a property such as the elastic thickness (e.g., McKenzie & Nimmo 1997; Crosby & McKenzie 2005), which is a proxy for the mechanical thickness of the lithosphere, which is in turn dependent on the geothermal gradient and the planetary heat flux.

In order to extract short-wavelength information in the (especially low-altitude) tracking data, we have developed an analysis method based on LOS acceleration data. Our aim in this analysis is to investigate whether we can locally improve the gravity models by using a different representation. We convert the Doppler residuals into LOS accelerations and then proceed with the estimation of a gravity field expressed in standard global spherical harmonics. We will show that models based on LOS data can have improved localized correlations with topography. We then use such LOS models for a localized analysis of admittance for four areas on Mercury where correlations with topography are noticeably high.

This paper is structured as follows. We introduce the LOS analysis method in Section 2. We show the gravity field model results using this analysis method in Section 3. We then use these gravity field models for an analysis of admittance for four selected areas, and we present the results in Section 4. We discuss our results in Section 5 and end with our conclusions in Section 6.

2. LOS Analysis Method

The determination of the gravity field models and related parameters from spacecraft tracking data is based on the precise determination of the spacecraft’s orbit. The differential equations describing the orbit are numerically integrated over a continuous span of time (called an arc) using high-fidelity models for the forces acting on the spacecraft, as well as for the measurements. The modeled measurements can be compared to the actual measurements, and their discrepancy (residuals) can be used to determine the parameters of interest that describe the forces and measurements using a batch least-squares method to iteratively minimize the residuals (e.g., Montenbruck & Gill 2000; Tapley et al. 2004).

The analysis of MESSENGER tracking data in Genova et al. (2019) was based on a technique where the equations of motion for the MESSENGER spacecraft and Mercury itself were numerically integrated simultaneously, with the goal to determine the parameters related to Mercury and its orbital dynamics (Genova et al. 2018). In our analysis, we use the same method of Genova et al. (2019), with the exception that while we still simultaneously integrate both orbits numerically,

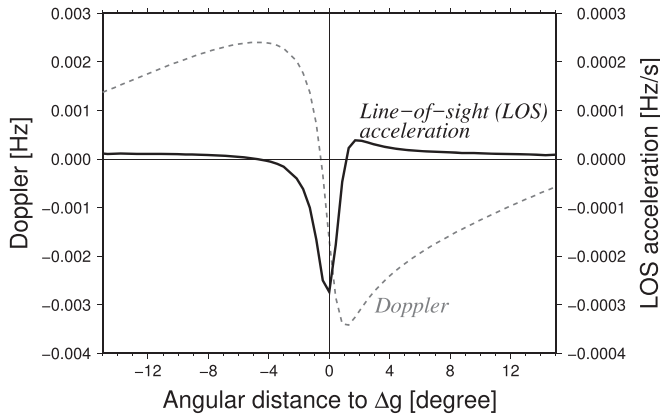


Figure 2. Influence of a 1° by 1° gravity anomaly Δg of 10 mGal on normal Doppler data and LOS accelerations.

we now use the updated Mercury ephemeris from Genova et al. (2019) for each arc and no longer estimate it. We refer to Genova et al. (2018, 2019) for the details about the processing of MESSENGER data. We use the NASA Goddard Space Flight Center GEODYN II Orbit Determination and Geodetic Parameter Estimation Program (Pavlis & Nicholas 2017), which has been used extensively for many years to analyze Earth and planetary orbiter tracking data.

The gravitational potential U is expressed in spherical harmonics (Kaula 1966) by

$$U(r, \lambda, \phi) = \frac{GM}{r} \sum_{n=0}^{\infty} \left(\frac{a_e}{r} \right)^{nm} \sum_{m=0}^n (\bar{C}_{nm} \cos(m\lambda) + \bar{S}_{nm} \sin(m\lambda)) \bar{P}_{nm}(\sin \phi), \quad (1)$$

where r , λ , and ϕ are the spherical coordinates radius, longitude, and latitude of the point where the potential is to be computed, respectively, and a_e is the reference radius of the planet. We use a value of 2440 km for Mercury. The gravity coefficients \bar{C}_{nm} and \bar{S}_{nm} are the normalized harmonic coefficients of the expansion of degree n and order m , and \bar{P}_{nm} are the normalized associated Legendre functions. We use the standard 4π normalization that is used in geodesy (Kaula 1966), which is given by

$$\bar{P}_{nm}(\sin \phi) = \sqrt{(2 - \delta_{0m})(2n + 1) \frac{(n - m)!}{(n + m)!}} P_{nm}(\sin \phi), \quad (2)$$

where δ_{0m} is the Kronecker delta, which is 1 when $m = 0$ and zero when $m \neq 0$. The gravity coefficients \bar{C}_{nm} and \bar{S}_{nm} are normalized using $\bar{C}_{nm} \bar{P}_{nm} = C_{nm} P_{nm}$ (and the same holds, of course, for the S_{nm} coefficients). In our analysis, we used the same starting gravity field model that was used to determine the HgM008 model.

Up to this point, our analysis is no different from previous analyses of MESSENGER tracking data. We process the Doppler data and generate partial derivatives of the measurements with respect to the estimation parameters (see Section 3.1 for more details), such as the coefficients of a gravity field model expressed in spherical harmonics. Our next step, however, is different from standard analysis, as we transform the Doppler residuals into LOS accelerations. These LOS data have a better sensitivity to local features, which will enable us to improve the gravity field at short wavelengths. We demonstrate the LOS sensitivity in Figure 2, where we show the influence of a gravity anomaly of 10 mGal ($1 \text{ mGal} = 10^{-5} \text{ m s}^{-2}$) at the surface of

size 1° by 1° on both Doppler data and LOS data, collected from an orbit with its pericenter at 40 km above the surface. The signal for the standard Doppler data is broad, whereas the signal for the LOS data is much narrower. In other words, anomalies further away from the LOS residual affect that residual less, whereas the Doppler signal gets smeared over a larger area. The LOS data localize the gravity signal better and are thus expected to more readily extract local signals.

We generate the LOS data from the standard Doppler residuals through numerical differentiation. We fit a cubic spline (smooth, piecewise polynomial) with natural boundary conditions through a time series of Doppler residuals and take the derivative of this spline to compute the LOS acceleration. This requires the Doppler data to be separated into passes; only one distinct combination of uplink and downlink station (called either two-way data when both stations are the same or three-way data when they are different) is processed at a time to ensure that proper LOS accelerations are computed. We apply the same differentiation to the system of partial derivatives of measurements with respect to estimation parameters in order to obtain a consistent set of observation equations. We then form systems of normal equations (see Section 3.1) from these new partial derivatives and LOS accelerations.

3. Results for Gravity Field Model Estimation with LOS Accelerations

The MESSENGER tracking data were analyzed as outlined above. We compare solutions using Doppler data (which we will call standard models) to solutions using LOS data (called LOS models). Konopliv et al. (2020) presented solutions in spherical harmonics of degree and order 160 because of the sensitivity of the low-altitude data to small-scale features. We present solutions up to degree and order 180 and discuss the merits of these larger expansions below. Solutions at such a high resolution require stabilization in the form of regularization, and this is also discussed. Before discussing the results of our analysis, we first outline the general estimation procedure.

3.1. Least-squares Solution

As mentioned in Section 2, we use linearized least-squares to estimate the spherical harmonics coefficients of a gravity field model. In gravity field determination, this often requires the use of regularization, i.e., the use of a priori information to stabilize or smooth the solution. If the noise on the data has a covariance W^{-1} , and we assume the use of a priori information \mathbf{x}_A with covariance \mathbf{P}^{-1} , then the k th iteration of the solution $\Delta \mathbf{x}_k$ can be found through (e.g., Montenbruck & Gill 2000; Tapley et al. 2004)

$$\Delta \mathbf{x}_k = (\mathbf{A}_k^T \mathbf{W} \mathbf{A}_k + \lambda \mathbf{P})^{-1} (\mathbf{A}_k^T \mathbf{W} \mathbf{r}_k + \lambda \mathbf{P} (\mathbf{x}_A - \mathbf{x}_k)), \quad (3)$$

$$\mathbf{x}_{k+1} = \mathbf{x}_k + \Delta \mathbf{x}_k,$$

where \mathbf{A}_k is the partial derivative matrix that was mentioned in Section 2 evaluated at current solution \mathbf{x}_k , λ is a Lagrange multiplier (which can also be seen as a weight factor on the constraint), \mathbf{r}_k are the current residuals, and $\Delta \mathbf{x}_k$ is the adjustment to the current solution. Partial derivatives are constructed from the numerical integration of the variational equations, which express the sensitivity of the data residuals with respect to changes in the estimated parameters. We refer to textbooks such as Montenbruck & Gill (2000) and Tapley et al. (2004) for a

Table 1
Variance Component Estimation Scale Factors

Data Set	Standard Solution	LOS Model
1	0.859	19.467
2	0.855	18.793
Low	0.879	19.004
Flyby	1.642	3.266

detailed description. The system in Equation (3) is called the normal equation system, with the conditioned normal equation given as $A_k^T W A_k + \lambda P$. This thus consists of two parts, one part ($A_k^T W A_k$) describing the data and the other (λP) describing the constraint.

The constraint often applied in gravity field determination assumes that the expectation for the coefficient values is zero ($x_A = 0$), with a variance of K/n^2 , where K is a constant depending on the planet (Kaula 1966). We also refer to Ermakov et al. (2018) for a discussion about power laws for gravity and topography. In Equation (3), this means that P is a diagonal matrix with entries n^4/K^2 on the diagonal, where n is the specific degree of the corresponding coefficient in x . For our solutions, we applied the Kaula constraint for degrees $n \geq 10$.

For the standard model, we used the same constant as HgM008, $K = 4 \times 10^{-5}$. However, we use a different factor for the LOS models. There is a difference in the magnitude of the residuals when comparing Doppler to LOS data (see Figure 2). The data part of the normal equation contains the weight matrix W , and we did not update this when transforming the system from Doppler to LOS. As a result of the difference in magnitude in the residuals, the diagonals of the data parts of the standard and LOS system differ in magnitude, ranging between a factor of 20 and a factor of 1×10^{-7} on an element-by-element basis, with the latter being much more prevalent. We thus found that the use of a standard value of K would result in an LOS model that overly conforms to a Kaula rule at the expense of fitting the data. In other words, using the standard Kaula constraint would overconstrain the solution because relatively, the constraint would contribute more information to the normal equation system in the case of the LOS solution. Rather than reweighting the data, we opted to reweight the constraint contribution (by using λ in Equation (3)) because this is a simple diagonal matrix.

We investigated a variety of factors and used $K = 17.9 \times 10^{-5}$ as the nominal factor for our LOS models, as that provided power spectra (see the next section) that are similar to the standard models. This factor was determined from applying a weight of 0.05 to a Kaula matrix with $K = 4 \times 10^{-5}$. We discuss additional weight factors in Section 3.3.

We also apply variance component estimation (Kusche 2003) to determine the scale factors on sets of normal matrices. We divide the set of MESSENGER orbital tracking data into three periods based on periapsis altitude and include the flyby data as a separate set. We show the periapsis altitude history of MESSENGER in the Appendix in Figure A1, and the resulting factors are listed in Table 1. The Appendix referred to here and throughout can be found at the data repository for this paper, Zenodo: [10.5281/zenodo.6547874](https://zenodo.org/record/6547874), as well as at our data archive, <https://pgda.gsfc.nasa.gov/products/84>.

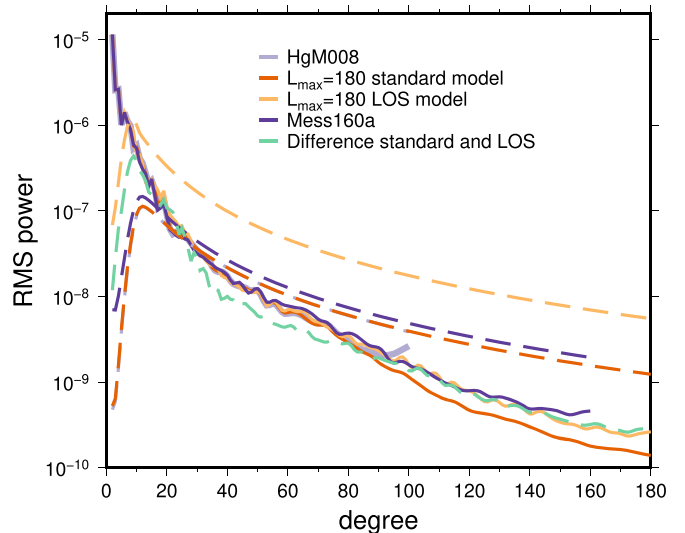


Figure 3. The rms power per degree for various gravity field models. Dashed lines indicate the error curves for each model.

3.2. Power Spectra and Gravity Anomalies

In Figure 3, we show the rms power spectrum per degree $p(n)$ of different gravity field models. This is expressed following

$$p(n) = \sqrt{\frac{\sum_{m=0}^{m=n} (\bar{c}_{nm}^2 + \bar{s}_{nm}^2)}{2n+1}}. \quad (4)$$

Despite small-scale differences between HgM008 and the standard model, their power spectra are virtually the same. The only difference is around degree 100, because the standard model has a larger maximum degree. Signals of aliasing and leakage such as are present in HgM008 (shown by an uptick in power at the higher end of the spectrum) are much less present, if at all, in the new models due to the larger expansion. The spectrum for the LOS model follows that of HgM008 and the standard model but deviates for a range of degrees around $n=20$ and then for $n > 60$. The LOS model may have decreased sensitivity with respect to the lower degrees than models based on Doppler data due to the enhanced sensitivity with respect to small-scale features that the numerical differentiation achieves. For comparison, we also include the power spectrum of the Mess160a model, and the LOS model follows this spectrum.

Figure 3 includes the error power spectra, which are also computed from Equation (4) by using the formal errors for the coefficients (which are obtained from the covariance matrix of the estimation process; see Equation (3)) instead of the coefficient values themselves. The error spectra for HgM008 and the standard model are indistinguishable and close to that of Mess160a, except for the lower degrees. The error spectrum for the LOS model, however, is very different, with much larger formal errors. This is related to the regularization that was applied. Not updating the weight matrix for the LOS data likely results in much larger formal errors because the covariance depends strongly on this. The formal errors for the LOS model are thus probably too conservative. The errors are already quickly larger than the coefficient values themselves, which would indicate coefficients that are indistinguishable from zero. However, as we will show in the next section,

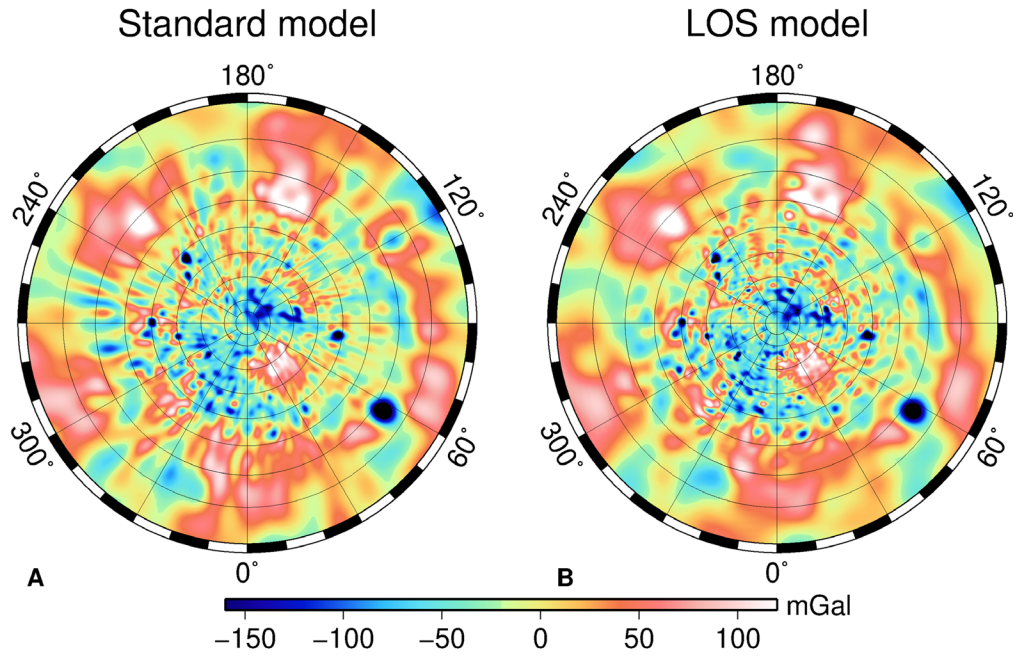


Figure 4. Gravity anomalies for a standard solution based on Doppler data (A) and for a solution based on LOS data (B). Both solutions are expanded to their maximum degree and order of 180. The projection is the same as that for Figure 1.

we have independent evidence that at higher degrees, the LOS model performs better than the standard model in areas where low-altitude data were available.

We also include the rms power of the coefficient differences between the standard and LOS model, and this spectrum only has large differences in some of the lower degrees. This is expected because, as mentioned above, the LOS signal is better at localizing small-scale features and may have decreased sensitivity with respect to the lower degrees. For higher degrees, the rms power of the differences is well below the formal errors of the other models, indicating that the formal errors of the LOS model are indeed too high.

Finally, we present solutions expressed in terms of gravity anomalies in Figure 4. These gravity anomalies Δg are defined by $\Delta g = -\partial U/\partial r - 2U/r$ (Heiskanen & Moritz 1984). The standard model shows streaks in its anomaly map that are along orbital ground tracks. Careful editing was applied, and residual tracks with an anomalously high residual signal were not included, yet some tracks may still result in streaks in the maps due to correlations with other parameters (such as the state vector). The standard model itself is close to the HgM008 model, but there are some differences due to the data editing applied. The LOS model, on the other hand, appears to be smoother. Streaks such as are visible in the standard model around 240°E are not present in the LOS model. The gravity signal closer to the equator appears to be smoother as well for the LOS model. Data closer to the equator have a higher spacecraft altitude, and this affects the LOS sensitivity; they cannot resolve smaller-scale features but also do not seem to introduce spurious signal, especially in terms of narrow north-south features, or latitudinal anomalies/streaks.

3.3. Regularization, Correlations with Topography, and Model Resolution

At a glance, the anomaly map of Figure 4(B) that shows the LOS model appears to have more circular features than the map of the standard model in Figure 4(A). This can be tested

quantitatively by computing the correlations between topography and gravity, where, in general, a model with higher correlations for higher degrees is deemed better, since it is expected that at small scales, gravity is primarily the result of topography (e.g., Wiczeorek 2015). In this section, we discuss these correlations together with the topic of model resolution and regularization because the latter two influence the former.

Correlations $\gamma(n)$ per degree between two spherical harmonic expansions with coefficients $(\bar{C}_{A, nm}, \bar{S}_{A, nm})$ and $(\bar{C}_{B, nm}, \bar{S}_{B, nm})$ are computed using the cross-power $S_{AB}(n)$ following (e.g., Wiczeorek 2015)

$$S_{AB}(n) = \sum_{m=0}^{m=n} (\bar{C}_{A, nm}\bar{C}_{B, nm} + \bar{S}_{A, nm}\bar{S}_{B, nm}),$$

$$\gamma(n) = \frac{S_{AB}(n)}{\sqrt{S_{AA}(n)S_{BB}(n)}}. \quad (5)$$

Global correlations between gravity and topography are shown in Figure 5(A), and they indicate that there is only a small difference between HgM008 and the standard model. They also show that, overall, the global correlations for the LOS model are below those for the other two models, indicating that despite appearances, it does not capture the topographic signal as well as the other two models. The correlations are especially low in the lower degree range 10–20, where we also find large differences in coefficient power (see Figure 3). This is likely due to less sensitivity of the LOS data to the lower degrees, as mentioned before; with half the sphere lacking in data, and with decreased sensitivity as the spacecraft has a higher altitude, we do not necessarily expect the global correlations to improve. Also, we applied the Kaula constraint for degrees $n \geq 10$, and this may further compound the insensitivity issue in this degree range. However, we emphasize that our goal was to investigate the models locally. We thus applied a localized analysis (Wiczeorek & Simons 2005, 2007; Simons & Dahlen 2007), and we show results focused on the area with low-altitude data in Figure 5.

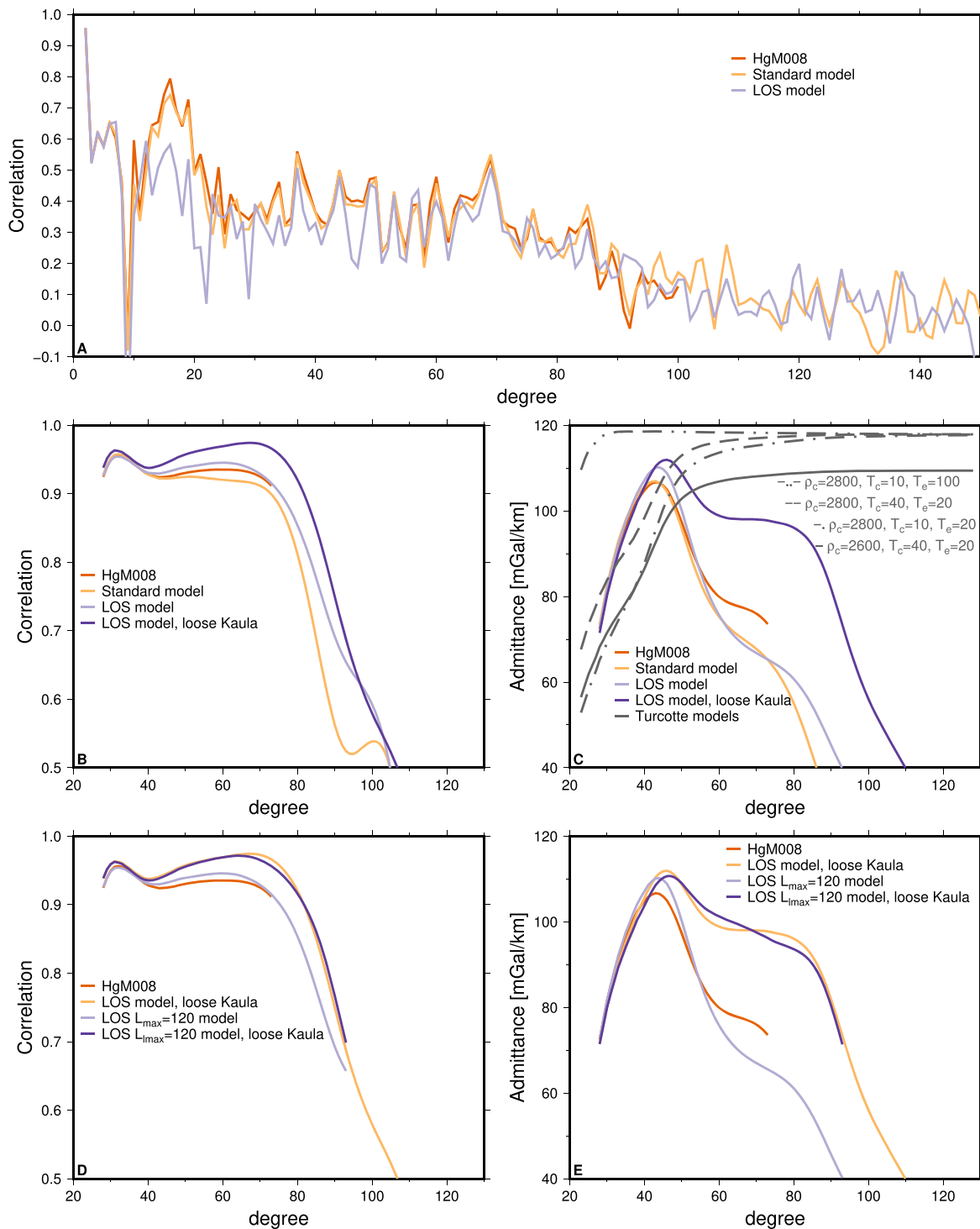


Figure 5. Global (panel (A)) and localized correlations between gravity and topography (panels (B) and (D)) and admittance (panels (C) and (E)) for various gravity field models. For the localized correlations, we show models with different Kaula rules applied (panels (B) and (C)) and models with different resolution (panels (D) and (E)). In one of the admittance plots (panel (C)), we also include theoretical curves following Turcotte et al. (1981) using different values for the crustal density ρ_c [kg m^{-3}], crustal thickness T_c [km], and elastic thickness T_e [km] to show the dependency on these parameters. The localization is centered on 270°E , 50°N with a radius of 15° and a windowing bandwidth $L_{\text{win}} = 22$.

Localized correlations and admittance were computed using a single taper for a spherical cap with a radius of 15° centered on 270°E , 50°N using a windowing bandwidth of $L_{\text{win}} = 27$ such that the taper has a concentration factor of 99.99% (Wieczorek & Simons 2005).

In Figures 5(B)–(E), we compare localized correlations and admittance for HgM008, the standard model, and the LOS

models. Correlations with topography are generally high for this area, above 0.9. The standard model has lower correlations than HgM008 for this area (although still above 0.9), but the admittance signal is very similar, except at the higher degrees. Small differences in the anomaly map (shown in Figure A2) likely result in decreased correlations. The LOS models have higher correlations with topography than the standard model

and HgM008, and, as Figure A2 shows, they show fewer stripes in the gravity map. These increased correlations with topography, which are an independent measure to evaluate the gravity field model, thus indicate an improved model. Despite similar, or even lower, global correlations, the LOS models do show local improvements. This also strengthens our earlier observation that the formal errors for the LOS models are too conservative.

Konopliv et al. (2020) investigated a set of constraints in their analysis, and it should be noted that one of their solutions uses $K = 5 \times 10^{-5}$, which is 25% larger than our nominal value for the Doppler models. Looser Kaula constraints (i.e., those with a larger value for K) will increase the power of the solution. As mentioned earlier, we already used a looser Kaula constraint for our LOS model in order to have the model's power match more closely with that of standard models. We investigated looser Kaula constraints in more detail and found that this influences both the local correlations and the admittance of the solutions. Konopliv et al. (2020) noted that their models have higher localized admittances compared to earlier models. In Figures 5(B) and (C), we include a result for an LOS model with a looser Kaula constraint of $K = 80 \times 10^{-5}$ (resulting from applying a weight of 0.0025 to the Kaula matrix with $K = 4 \times 10^{-5}$). This model, while it will have spurious power for most of the areas, has improved correlations for this area. The admittance curve is also different in shape; it levels off at higher degrees instead of quickly decreasing. The quick drop in admittance for the other models is likely caused by the dominance of noise in the gravity field models, in addition to suppressed signal by a stronger Kaula constraint. A more level admittance is more in line with theoretical loading models (e.g., Turcotte et al. 1981). We show this in Figure 5(C) by including localized admittance following Turcotte et al. (1981). We include curves for different crustal densities, crustal thickness, and elastic thickness (see Section 4.2 for more details) to indicate dependency on these parameters. This means that the gravity field model with the looser Kaula constraint can be used while including higher degrees in an admittance analysis, which improves the determination of parameters from such an analysis.

Following Konopliv et al. (2020), we increased the resolution of our models from the initial size of HgM008 of degree and order 100 to solutions with a maximum degree of 180. Intermediate solutions had a resolution of degree and order 120, and judging from the correlations with topography as presented in Figure 5, the solutions' effective resolution, where correlations are still high enough, would be up to degree 80 (for the localized spectrum). However, we noticed that especially the admittance can be influenced by the model resolution, and we show this in Figures 5(C) and (D), with models of a lower resolution of degree and order 120. While the correlations are not different between the models of different resolution, the admittance for the degree and order 120 model is not as level as that for the degree and order 180 model. The differences are not very big, but at these higher degrees, the admittance is expected to be more or less flat. Hence, we will use the degree and order 180 LOS model with the relaxed Kaula constraint in our analysis of admittance.

4. Admittance Analysis

We now use our LOS model in an analysis of admittance to determine properties of the lithosphere. The focus is on four

different areas, where correlations between gravity and topography are high. The areas are introduced here, together with the chosen admittance model. We then show the results of estimating parameters by fitting the admittance in a least-squares sense for each area.

4.1. Area Selection

The models and LOS technique were developed with the goal to improve the gravity field model locally. We use global spherical harmonics because they are widely used in geophysics, but we stress that our model with the relaxed Kaula constraint of $K = 80 \times 10^{-5}$ is to be used only locally. In areas where especially the altitude of the spacecraft was low and tracking data were collected, it will perform well, but it will show spurious signal in other areas.

To select the areas we investigate, we performed a localized analysis of gravity and topography. We computed localized correlations (and admittance) for spherical caps with a radius of 15° centered on points at intervals of 5° in both latitude and longitude, covering the entire planet. For this analysis, we used a windowing bandwidth of $L_{\text{win}} = 22$ such that each taper has a concentration factor of 99.9%. Most of the energy of the taper will be concentrated in a smaller area around the center coordinates. For each spectrum, we compute the average correlation $\bar{\gamma}$, which we weigh with a weight w_n that relates how much this correlation deviates from a threshold value γ_T , following

$$w_n = \frac{1}{(\gamma(n) - \gamma_T)^2},$$

$$\bar{\gamma} = \frac{\sum_n w_n \gamma(n)}{\sum_n w_n}. \quad (6)$$

Here we use $\gamma_T = 0.9$, and this enables us to readily identify areas that have correlations close to 0.9 without having the average be adversely affected by low correlation values in a spectrum. We note that areas with only a few degrees with correlations close to 0.9 will also produce high average correlations. We choose a threshold value of 0.9 in order to satisfy as closely as possible the assumption that correlations between gravity and topography are unity in the theoretical models (see Section 4.2). Correlations can also be related to a measure of the signal-to-noise ratio (S/N) per degree, $S/N(n)$, under the assumption that deviations from unity correlations are caused by unmodeled gravity signals that are not correlated with topography, following (Grott & Wiczeorek 2012)

$$\gamma(n) = \left(1 + \frac{1}{S/N(n)}\right)^{-\frac{1}{2}}. \quad (7)$$

For correlations of 0.9, the S/N is 4.26.

In Figure 6, we show the result of mapping the average correlations for each spectrum and indicate the four areas that we selected. We also include a map of the topography to show the context of the areas. We only highlight average correlations higher than 0.8 (an S/N of 1.8), and most are lower than this. Several areas, however, do show clusters of higher correlations. If we set the threshold value γ_T to 1.0 instead of 0.9, the areas with high average correlations decrease in size but are in the same locations (Figure A3). The areas in northern latitudes and the western hemisphere are related to areas where low-altitude

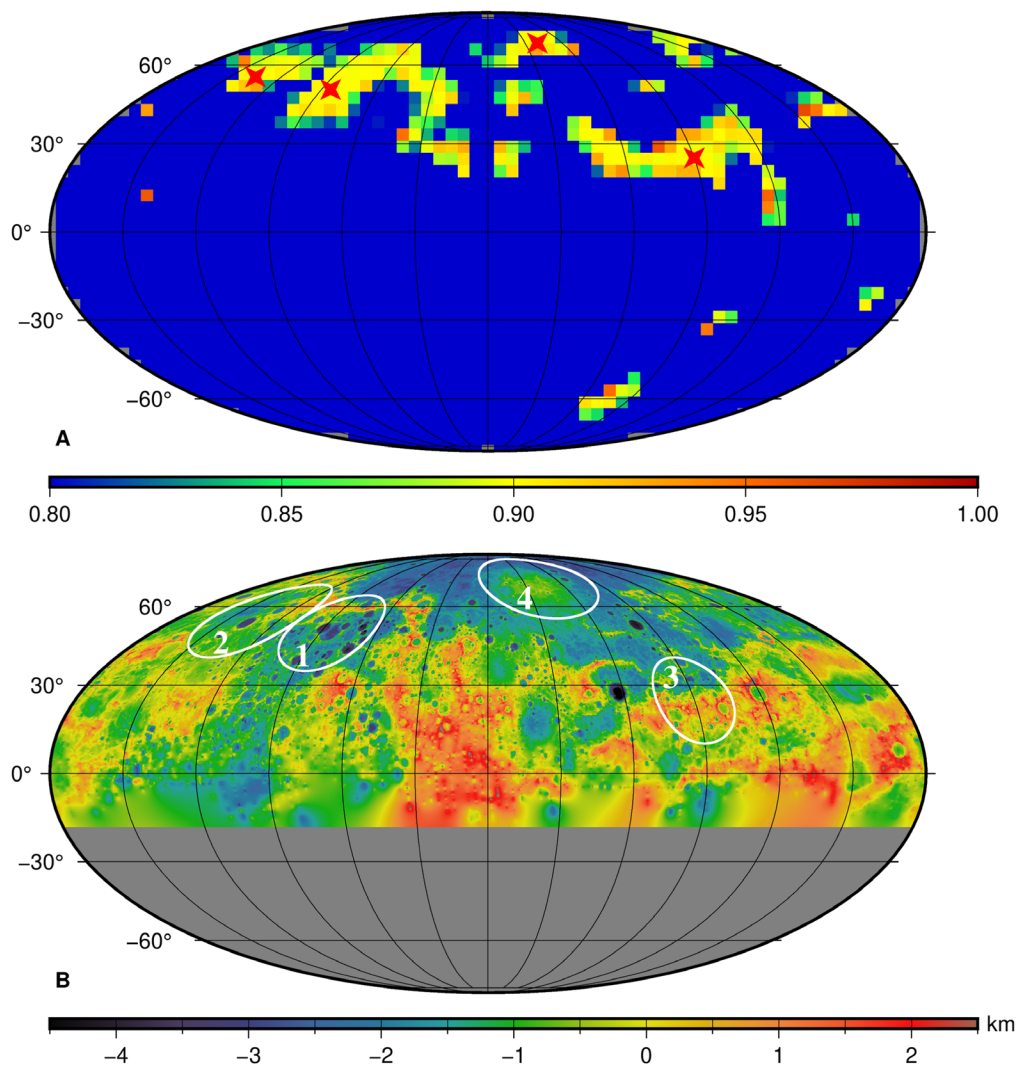


Figure 6. Averaged correlations weighted by their deviation from 0.9 (A) and topography from MLA, with the southern hemisphere where no MLA data were collected masked in gray (B). Both maps indicate the chosen locations for areas with high average correlations (stars in the top map, numbers in the bottom map). In the topography map, we include the spherical caps with a radius of 15° that we use in the localizations. The maps are in Mollweide projection centered on the prime meridian.

tracking data were collected (like our sample area in Figure 5) and are thus of special interest. We select two areas there, both in cratered terrain, as can be seen in the topography map. We also select two more areas: one in a lower-latitude area with more pronounced topography and one focused on the feature known as the northern rise, recognized in both topography (Zuber et al. 2012) and gravity (Smith et al. 2012) early on during MESSENGER’s mission. In Figures A4–A7, we show the topography and gravity anomalies for each area.

For each selected area, we choose the central locations such that all surrounding grid cells (which are 5° by 5° because of our spacing) also have a weighted average correlation better than 0.9. This results in the following central locations: area 1 is centered on 275°E , 50°N ; area 2 on 225°E , 55°N ; area 3 on 90°E , 25°N ; and area 4 on 40°E , 70°N (northern rise). In Figure 5, we showed that the correlations with topography are higher for the LOS model compared to the standard model for area 1. For area 2, the correlations are also (slightly) higher for the LOS model, and they are very similar for both models for areas 3 and 4.

As stated before, a high average correlation may mean that only a few degrees of the spectrum have a correlation close to the threshold, 0.9, which would make the spectrum less suitable for admittance analysis. Upon inspection of the spectra of areas 3 and 4, we found that when using $L_{\text{win}} = 22$, the range of degrees with high correlations is limited (Figure A8). We opted to increase the cap radius to 30° , decreasing L_{win} to 8 to still obtain a concentration factor of 99% for the first taper. As stated above, the energy is still mostly concentrated in a smaller area around the center coordinates. For area 3, this means that it still covers an area with high topography, and for area 4, it includes a slightly wider area covering the northern rise. In addition, because of a relatively high admittance for the loose Kaula model (Figure A9), we opted to use the standard model for area 3 in the admittance analysis.

The admittance and correlations for these areas are shown in Figure 7. For each area, we selected a degree range that will be used when estimating the lithospheric parameters. This degree range is indicated in Figure 7. For areas 1 and 2, because of high correlations over a large degree range, we limited the correlations to be above 0.9. For areas 3 and 4, however,

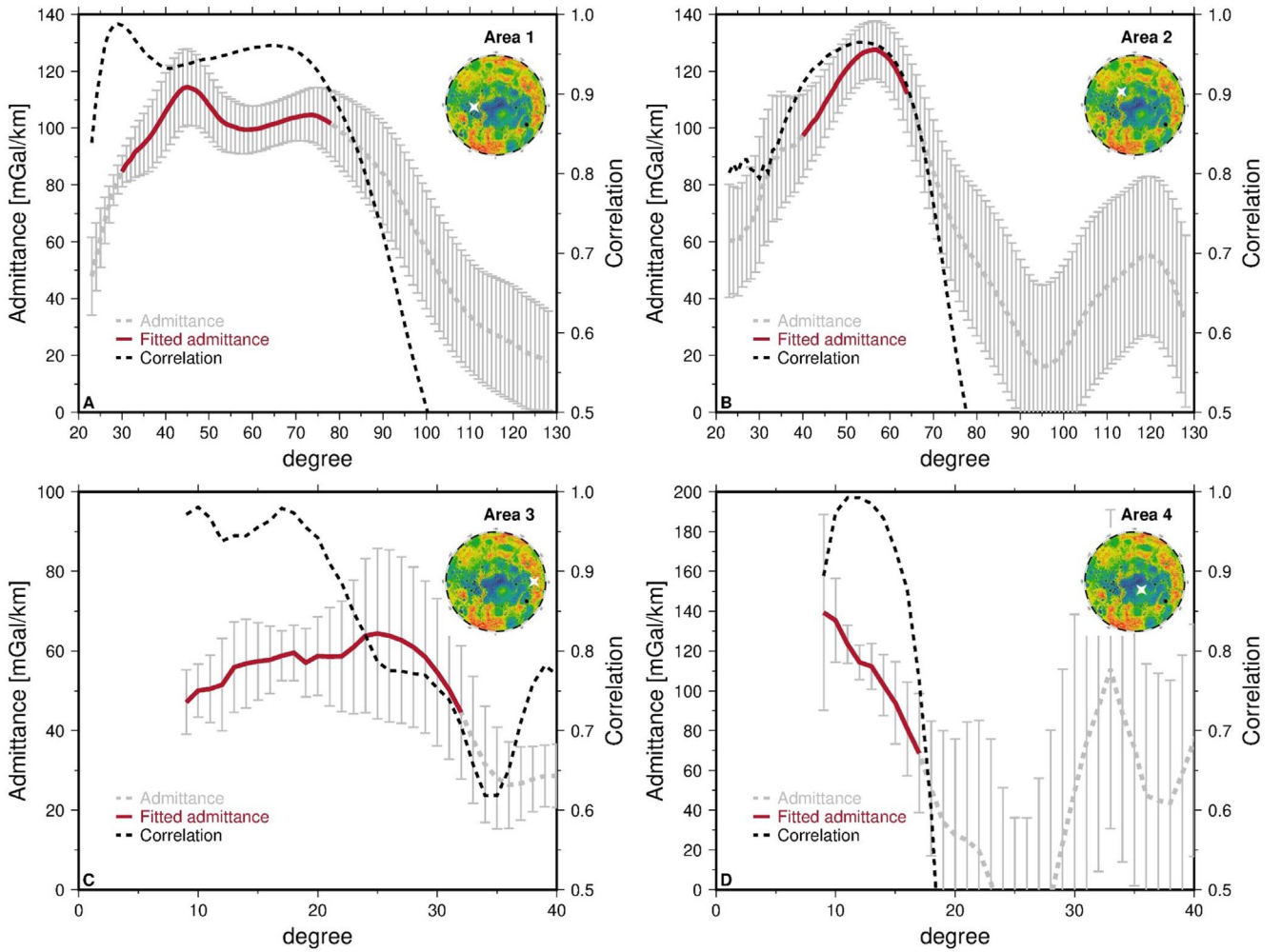


Figure 7. Localized admittance and correlation spectra for the areas that we selected. Correlations are shown with black dashed lines, and admittance is shown in gray. For areas 1 and 2, the localization used $L_{\text{win}} = 22$, and for areas 3 and 4, $L_{\text{win}} = 8$ was used. For each area, we select a degree range that will be used in the admittance analysis. The admittance over this degree range is shown with a red solid line. We indicate the location of each area on a north pole-centered stereographic map of topography. Admittance errors are indicated with error bars and are three times the error computed from Equation (8).

despite narrowing the windowing bandwidth, the correlations still drop quickly. For these two areas, we adopt a threshold of 0.7 in the correlations, which corresponds to an S/N of 1. This does not affect the results much, as most degrees in the range used have higher correlations and thus a higher S/N. The admittance also has a higher error for those degrees; thus, they are downweighted in our admittance analysis.

The variance of the admittance, $\sigma^2(n)$, is computed from the correlation with topography following Wicczorek (2008),

$$\sigma^2(n) = \frac{S_{\Gamma\Gamma}(n) (1 - \gamma^2(n))}{S_{\Phi\Phi}(n) 2n}. \quad (8)$$

Here Γ now represents the localized gravity and Φ the localized topography. In Figure 7, the error bars show three times the error, $\sigma(n)$, as computed from Equation (8), to use a conservative error estimate in our admittance analysis. We found that using the tighter, 1σ , error in our admittance analysis does not change the parameter distributions; overall, we just find fewer models that are accepted in our analysis.

Considering Equation (7), increasing the admittance error may also suggest that we implicitly adopt a lower S/N threshold, which could also mean that we could increase the degree range for our admittance fit. We choose not to do the

latter because the admittance models require high correlations between gravity and topography.

Finally, for area 3, the error at high degrees becomes very small (e.g., Figure A8A) because the gravity power $S_{\Gamma\Gamma}$ becomes small, whereas this is much less the case for the other areas. While unrealistic, this is in a degree range that we do not use in our analysis, and it does not affect our results.

4.2. Admittance Model and Parameter Estimation Procedure

We use the admittance model of Grott & Wicczorek (2012). Their model describes the effects on the gravity field of loads placed on and beneath the surface, and it relates gravity and topography through a transfer function $Q(n)$ in the spherical harmonics domain. Their function is dependent on a set of parameters that describe the densities and elastic properties of the lithosphere. This set of parameters is given by the crustal density ρ_c , the load density ρ_l , the mantle density ρ_m , the crustal thickness T_c , the elastic thickness T_e , the load depth z , and a load parameter L .

Loads are described by thin mass sheets with surface density σ_{nm} , and the subsurface load can be characterized by the ratio $f_{nm}^z = \sigma_{nm}^z / \sigma_{nm}^s$, where z refers to the subsurface load and s to loading at the surface. This ratio can depend on the degree and

order, but here it is assumed to be isotropic, and the subscripts can be dropped. Because f ranges between zero (top loading) and $\pm\infty$ (bottom loading with negative or positive loads), Grott & Wieczorek (2012) introduced the load parameter L ,

$$L = \frac{f}{1 + |f|}, \quad (9)$$

with L varying between -1 and 1 , where $L=0$ corresponds to top loading only, $L = \pm 1$ is bottom loading only, and $L = -1/2$ for $f = -1$ (the loads are the same but of different sign). For completeness, we list the equations that describe the model in the Appendix, Section A. Additional parameters in the model are the material properties of Young's modulus E and Poisson's ratio ν . We use standard values of $E = 100$ GPa and $\nu = 0.25$. The value for E is only really valid for intact rock, and modifications for deformed rock can be made that can result in values very different from the standard value (Klimczak et al. 2015). Our analysis is not that sensitive to values of E , or it would easily trade with subtle variations in T_e (see Section A1).

This admittance model was originally developed for Mars and applied to Tyrrhena Patera, and it has been applied to other volcanoes on Mars (e.g., Broquet & Wieczorek 2019). We use it here because it has several features that also apply to Mercury. The model of Grott & Wieczorek (2012) has both top and bottom loading, which are in phase. This means that correlations between gravity and topography are assumed to be one, and deviations from unity correlations can be used to infer errors on the admittance (Wieczorek 2008). This also makes it suitable to be applied to our areas of interest that have high gravity–topography correlations. In Grott & Wieczorek (2012), top loading can be considered as extrusive volcanic deposits, and subsurface loading can be considered as high-density rocks in the crust, under the volcano. To some extent, depending on the area on Mercury, a similar interpretation can be given. Otherwise, in cratered terrains, a crater that excavates crust is a negative top load, for example, and the loads can thus be interpreted in this way on Mercury.

Our main goal is to estimate geophysical parameters using our new gravity models locally. We leave several considerations for future analysis, such as the use of admittance models that are specifically constructed for Mercury with cratering, effusive volcanism, and dynamic mantle flow. We assume that top and bottom loading are in phase, and for now, we will not simultaneously fit admittance and correlation spectra, such as is done in, e.g., Audet (2014). We acknowledge that this may affect the estimated parameter distributions, but we stress that this is why we focus on areas where correlations between gravity and topography are high.

Our parameter estimation procedure is as follows. Initially, we explore a wide range of parameter values and perform a grid search to find the best-fit model in a least-squares sense. The parameters we vary are crustal density, load density, crustal thickness, elastic thickness, load depth, and load parameter. We set the planet radius to 2440 km and use a fixed mantle density of 3200 kg m^{-3} (e.g., Hauck et al. 2013). For each area, we first downward continue gravity to the average radius in that area, which is obtained from localization (see, for example, Wiecezorek 2008). We list the average radii for each area in Table 3 and note that they all are close to the average planet radius of 2440 km. We then compute the localized measured spectrum (as shown in Figure 7). We construct theoretical

Table 2
Parameters and Bounds Used in the MCMC Method

Parameter	Symbol	Unit	Lower Bound	Upper Bound
Crustal density	ρ_c	kg m^{-3}	1600	3200
Load density	ρ_l	kg m^{-3}	1600	3200
Crustal thickness ^a	T_c	km	2	150
Elastic thickness ^a	T_e	km	2	150
Load depth ^a	z	km	2	Crustal thickness
Load parameter	L	None	-1	1

Note.

^a To prevent instabilities, we use a minimum of 2 km for thickness or depth.

gravity models from admittance for the set of parameters and apply the same downward continuation and localization. We then compare the theoretical spectrum to the measured one by computing the misfit for the admittance over the selected range of degrees. We list this range for each area in the following sections.

Once we determine the best-fit model, we use it in an additional analysis using a Markov Chain Monte Carlo (MCMC) method (e.g., Mosegaard & Tarantola 1995). We refine our grid search by randomly perturbing the parameter values of the best-fit model. In Table 2, we list our estimated parameters and the bounds that we use in our MCMC analysis. For each model, a new theoretical admittance model is computed using the randomized parameters, and the localized admittance of this new model is tested against the measured admittance spectrum in a Metropolis–Hastings scheme (Metropolis et al. 1953; Hastings 1970). We compute a probability function $P(j)$ for each j th model from

$$P(j) = \exp\left(\frac{1}{2} \mathbf{dx}^T \mathbf{C}^{-1} \mathbf{dx}\right), \quad (10)$$

where \mathbf{dx} is the vector of admittance differences between the theoretical and the measured admittance at each degree, and \mathbf{C} is a diagonal matrix with the square of the admittance error from Equation (8) at each degree on the diagonal. In the MCMC algorithm, a model is accepted if the probability ratio $P(j)/P(j-1)$ is larger than a draw from a uniform distribution. We run a total of 200,000 models and do this separately 10–20 times (each is called a chain). We retain only the accepted models. The result is a set of parameters that produce admittance spectra that fit the measured spectrum within the computed errors per degree from Equation (8). As stated before, we take a conservative approach and multiply these errors by a factor of 3.

4.3. Results

We discuss the distributions for the parameters below. For each area, the MCMC analysis resulted in a set of models with their admittance within the specified errors. We show the fitted admittance spectra in Figure 8. We list the central values and their standard deviations for the estimated parameters in Table 3. This table also indicates the range of degrees that were used in the fits (see also Section 4.1). For areas 1 and 2, we used a localization cap radius of 15° and a windowing bandwidth of $L_{\text{win}} = 22$, whereas we used 30° and 8 for areas 3 and 4.

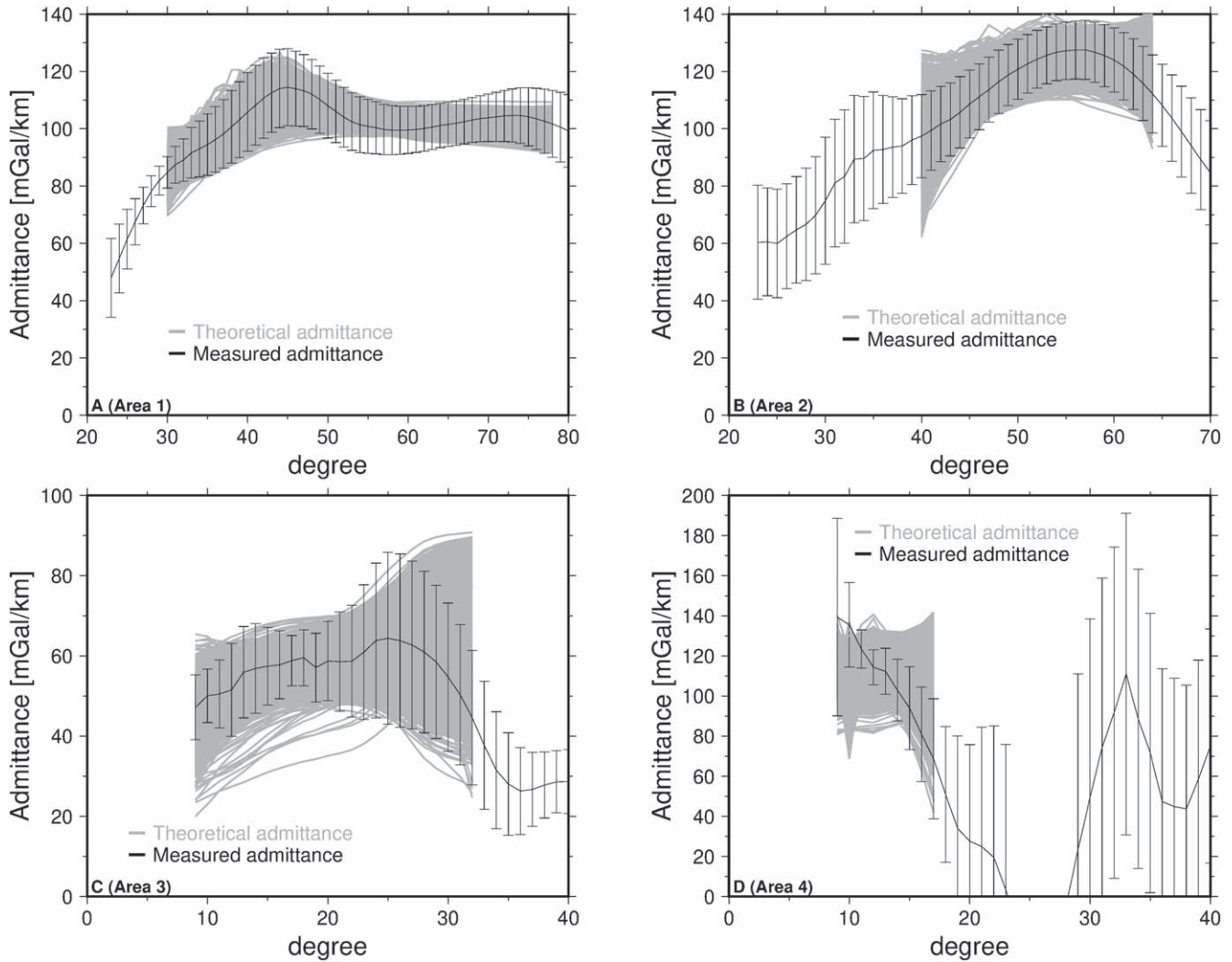


Figure 8. Fitted admittance spectra from our MCMC analysis for each area. The measured spectra are shown in black, and the spectra for the MCMC models over the degree range where correlations are high are shown in gray. The error bars are three times the errors from Equation (8).

For areas 3 and 4, we perform an additional analysis where we fix several of the parameters. We set the crustal and load density to be equal (thus representing an average crustal density) and use only the top-loading scenario (eliminating the depth and load parameters). We also fix the crustal thickness to a value of 40 km (see, for example, Beuthe et al. 2020a and Section 5.4), as we appear to be not that sensitive to crustal thickness variations, despite reasonably well-defined parameter distributions in our MCMC analysis. With this, we only have two parameters to adjust, the (crustal/load) density and elastic thickness.

In general, the spread for the parameter values in the distributions is large, as can be seen by the errors quoted in Table 3. This is likely to be due to the intrinsic nonuniqueness of the inversion, partly by fitting only a limited part of the spectrum, rather than our use of three times the errors on admittance. As stated earlier, using 1σ changes the number of models accepted in our MCMC analysis but not the distribution. This may make the interpretation of the values per area more difficult. Rather, we focus on the differences between the areas, which may indicate variations in Mercury’s lithospheric properties.

4.3.1. Results for Area 1: 275°E, 50°N

Area 1 is a cratered terrain, with the center close to the Stravinsky and Vyāsa craters, and it is located in the high-Mg region identified from MESSENGER X-ray spectrometer data (e.g., Weider et al. 2015). The gravity map shows gravity highs surrounding craters in a low terrain (Figure A4). We fit the admittance for the degree range 30–78. As can be seen from Figure 8(A), the admittance matches the measured spectrum well over the entire degree range.

The parameter distributions from the MCMC analysis are shown in Figure 9. The admittance analysis finds a crustal density close to 2600 kg m^{-3} . The load density is lower, 1900 kg m^{-3} . The load parameter of 0.4 indicates that subsurface loading is present. The load depth is about midway in the crust. We discuss the load and sensitivity (in general, for all of the areas) in more detail in Section 5.1. We find an elastic thickness of 28 km for this area.

As expected, the spread for most of the parameters is large, with a wide range of densities and crustal thicknesses allowed. Only the elastic thickness appears relatively well determined, having a narrow distribution. For this particular spectrum, the correlations with topography are high over a relatively wide

Table 3

Results for the Central Values and Standard Deviation for the Lithospheric Parameters per Area, Localization Radii, Admittance Degree Range, and Fit

Parameter	Area 1	Area 2	Area 3	Area 4
Crustal density [kg m^{-3}]	2622 ± 190	2410 ± 205	2488 ± 160	2793 ± 146
Load density [kg m^{-3}]	1905 ± 152	2156 ± 192	2033 ± 168	2924 ± 135
Load depth [km]	37 ± 14	68 ± 17	40 ± 16	29 ± 13
Crustal thickness [km]	65 ± 15	53 ± 20	112 ± 17	36 ± 14
Elastic thickness [km]	28 ± 7	15 ± 10	11 ± 7	23 ± 11
Load parameter [none]	0.39 ± 0.12	0.53 ± 0.17	0.25 ± 0.11	0.06 ± 0.05
Average radius for localization [km]	2438.332	2438.937	2439.519	2438.328
Admittance fit degree range	30–78	40–64	9–32	9–17
Admittance fit [mGal km^{-1}]	5.51 ± 1.03	6.61 ± 1.80	8.08 ± 2.57	26.37 ± 1.92
Best fit [mGal km^{-1}]	2.16	1.10	3.38	10.98

range of degrees, and the admittance itself is relatively flat at the higher degrees, which is what the theoretical models predict. By including the (to some extent) lower degree range where the admittance is increasing, sensitivity with respect to the elastic thickness is obtained, as that mostly has an influence on the lower degrees.

4.3.2. Results for Area 2: 225°E, 55°N

Area 2 covers the Strindberg crater and also shows a mix of gravity highs and lows (Figure A5), similar to area 1. It also covers some lobate scarps (e.g., Watters et al. 2015). The theoretical models again fit the measured spectrum well over the entire range of degrees (Figure 8(B)). While the degree range for this area is not as wide as for area 1, there are many similarities between the two areas, as can be seen from both the admittance curve and anomaly map.

The parameter distribution is shown in Figure 10. The results in terms of the parameter distributions show some differences from those for area 1. The densities are marginally consistent with those of area 1 (see Table 3), but the distribution has considerable overlap. The crustal thickness is consistent between the two areas, but the elastic thickness is lower for area 2. The peak at very small values for T_e corresponds to lower load factors L ; without this peak, the average value for T_e would be closer to that of area 1, at around 20 km.

4.3.3. Results for Area 3: 90°E, 25°N

Area 3 covers both high and low topography in heavily cratered terrain in the area of the Hafiz and Munkácsy craters (Figure A6). The MCMC analysis results in models that fit this spectrum well (Figure 8(C)), yet at the higher degree values, the downward trend of admittance is not always captured, with accepted models falling outside the 3σ range.

The parameter distribution for this analysis is shown in Figure 11. We find a crustal density in line with that of the previous two areas, around 2500 kg m^{-3} . The elastic thickness is lower at 11 km and has a narrow distribution. The crustal thickness is considerably higher for this area, above 100 km. The load parameter indicates some subsurface loading, and the load density itself is low.

The narrower range of degrees (and differences in parameters when using a different degree range; see Section 5.1.2) makes the results for this area less robust than those for the previous two areas. We thus performed an analysis where we only estimate a density and elastic thickness,

keeping all other parameters fixed (as explained at the start of Section 4.3).

The distributions for these two parameters are shown in Figure 12. The average density and elastic thickness obtained from these distributions both decrease, to $2412 \pm 157 \text{ kg m}^{-3}$ and $5 \pm 3 \text{ km}$, respectively. The lower elastic thickness is likely a result of the choice for top loading only. The distribution for density overlaps with that from the case where all parameters are estimated. We only consider the density and elastic thickness results for this area to be robust.

4.3.4. Results for Area 4: 40°E, 70°N (Northern Rise)

Area 4 is centered on the northern rise in Mercury's smooth plains (Figure A7), and it is the only area in our set that focuses on a single feature. The admittance for this area is generally high (see also Figure A8B for the admittance using the smaller spherical cap), which could be indicative of dense materials beneath or in the crust. We noticed in the initial MCMC runs for this area that the crustal density can be higher than the load density, although not by very much. For the scenario of dense materials in the crust, we thus present results here where we enforce the load density to be larger than the crustal density. We also show the parameter distributions and admittance fits for the case where we do not enforce this in Figures A10 and A11, respectively.

The theoretical models fit the measured spectra (Figure 8(D)), but because of the relatively large error at the lower degrees, the initial downward trend in admittance is not captured very well. The models do match the trend at the higher end of the degree range. The parameter distributions for this area are shown in Figure 13. The results indicate a top-loading scenario (with the load parameter centered closer to zero than it was for the other areas), with higher densities than we find for the other areas. This is consistent with earlier observations (e.g., James 2018). The load parameter centering close to zero is also the result of enforcing that the load density has to be larger than the crustal density. When we do not enforce this, the load parameter is slightly larger than zero (Figure A10), and in that case, larger load parameters correspond to lower load densities. We also note that a load parameter different from zero is often needed to fit the downward trend in admittance at higher degrees. The load density is limited to be smaller than the mantle density, hence the cutoff in the histogram at 3200 kg m^{-3} in Figure 13(B).

For this area, we find a lower crustal thickness than for the other areas, but it should also be noted that some of our MCMC runs produce wider distributions for the crustal thickness,

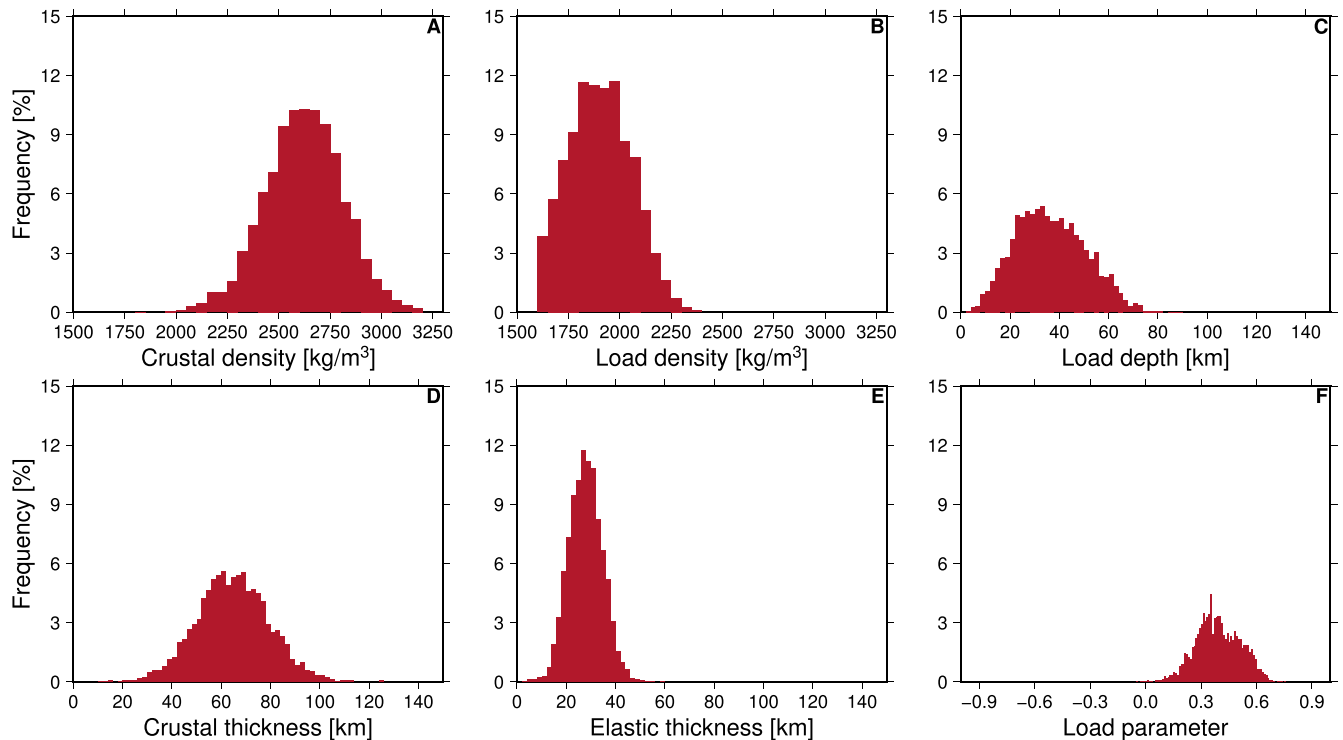


Figure 9. Results from the MCMC analysis for area 1, shown as a posteriori probability distributions for the estimated parameters: crustal density (A), load density (B), load depth (C), crustal thickness (D), elastic thickness (E), and load parameter (F).

indicating the results may not be as sensitive to this parameter. In those cases, the other distributions do not vary much. The elastic thickness is again relatively low but with a wider range than some of the other areas. Apart from differences in density and an insensitivity to crustal thickness in the results shown in Figure A10, the distributions for the other parameters are very similar, regardless of whether we enforce the load density to be larger than the crustal density.

For the northern rise, we also performed the analysis where we only estimate a density and elastic thickness. The distributions for these parameters are shown in Figure 14. This results in a narrow distribution for the density, with an average of $3158 \pm 26 \text{ kg m}^{-3}$ (again, the density was limited by the assumed mantle density). This density is higher than what we find when estimating more parameters, although it is within the distribution for the crustal density in Figure 13. (It is also closer to the load density that we find when using $L_{\text{win}} = 22$, as discussed in Section 5.1.2 and shown in Figure A12.) The elastic thickness distribution is consistent with that when we estimate more parameters. We consider the density and elastic thickness to be robust parameters in this analysis, together with the indication of top loading. The density results vary between the cases, but it is consistently higher than the density in the other areas, which is consistent with earlier analyses. We discuss the high densities for the northern rise in more detail in Section 5.2.

5. Discussion

The results of our admittance analysis indicate differences in the lithospheric properties for various areas on Mercury. For each area, the degree range used to fit the admittance is different, which may result in different sensitivities with respect to each parameter, and this may affect the robustness of our estimates. We discuss such sensitivities in this section. We also

briefly discuss the results for the northern rise and for our low elastic thickness values in terms of heat flux. We compare our results for crustal density and thickness to a recent analysis by Beuthe et al. (2020a).

5.1. Sensitivity of the Solutions

Our MCMC analysis results in distributions for the parameters that are mostly close to normal distributions (see Figures 9–14), albeit with large spreads. Yet because of the different degree ranges used, one can expect, for example, a parameter such as crustal density to be not as well determined as when higher degrees are included; at smaller scales, admittance will be less dependent on parameters such as elastic thickness, and it will be mostly determined by the crustal density (e.g., Wiczorek et al. 2013).

5.1.1. Parameter Variations

For each area, we conduct a sensitivity test. We take the theoretical model with the best fit to the admittance, and we then vary one parameter at a time while keeping the others fixed (at the best-fit values). This test shows that mostly, the results are sensitive to all parameters. If we vary one parameter, we see a clear minimum in admittance misfit. If our results were not sensitive to a certain parameter, we expect to see a flat admittance fit for a wide range of parameter values, but this is not the case. We show an example in Figure A13. For the elastic thickness example, we see a wide range of misfits close around the best-fit value. Further analysis shows that this is because of strong changes in the admittance curves for small changes in T_e (Figure A14). For larger values of T_e , the fit to the admittance levels off, but it is higher than the general level of fit (this is the case for the other areas as well), which means

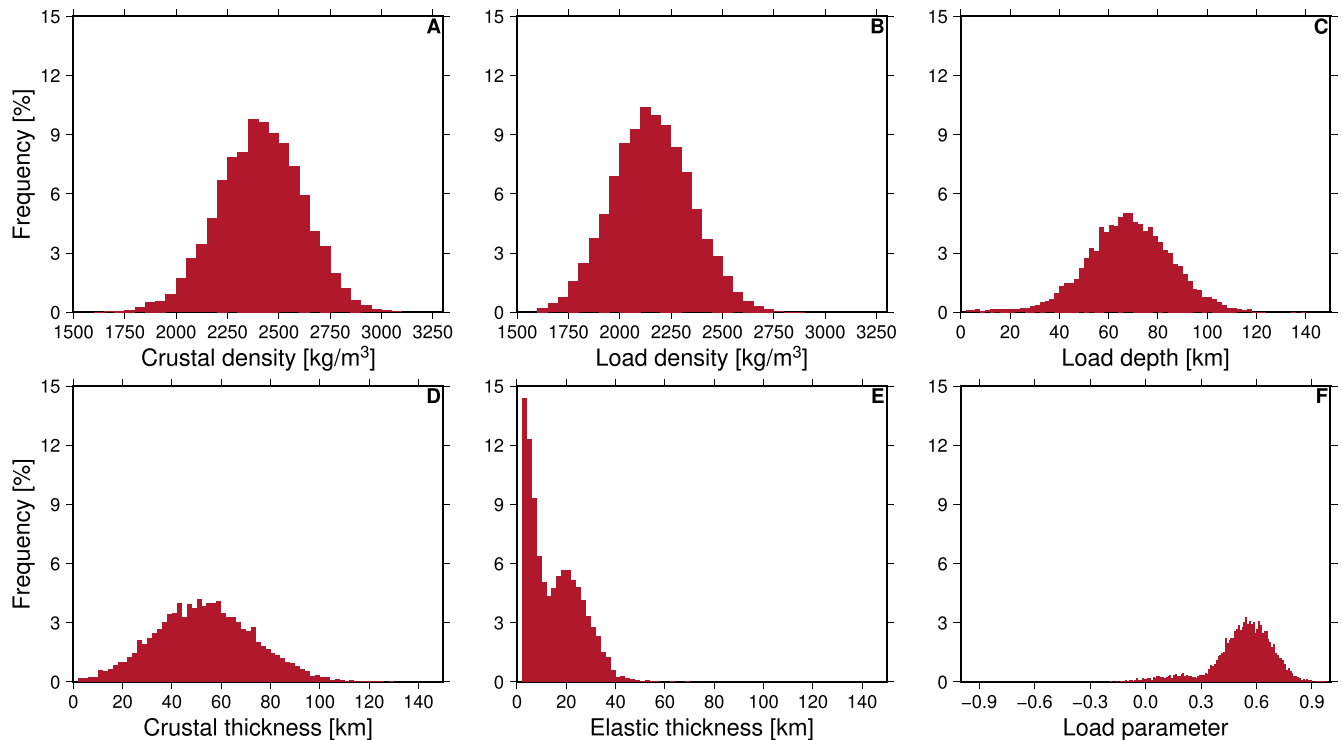


Figure 10. Results from the MCMC analysis for area 2, shown as a posteriori probability distributions for the estimated parameters: crustal density (A), load density (B), load depth (C), crustal thickness (D), elastic thickness (E), and load parameter (F).

those models can be excluded (as indeed, in this case, Figure 10 shows).

For this particular example in area 2, the best-fit T_e value is 9 km, out of an evaluation of many models, while the histogram in Figure 10 shows peaks at a low value, 20 km, and a small one just above 40 km. We noted in Section 4.3.2 that a low T_e for this area correlates with low crustal densities and high crustal thickness values.

We also note that MCMC not only obtains a best-fit value but also maps out the models that fit the admittance over the chosen degree range within the given errors. Hence, the histogram for T_e in Figure 10 shows a much wider range for T_e , not even centered on this best-fit value of 9 km. The strong sensitivity seen in this test may also indicate an interdependency between the parameters for the admittance curves that produce the best fit; there is a set of best-fit values, and changing one by a small amount may change the admittance by a large amount. We investigated this in more detail by plotting the parameter values from our MCMC against each other in a triangle plot in Figure 15. This allows us to investigate the correlations between parameters. The results for area 1 in Figure 15 show that there are no strong correlations between the parameters because all two-dimensional a posteriori distribution plots (of one parameter versus another) are fairly circular. There is a negative correlation between load parameter L and load density, which is to be expected. The plots for the results for the other areas look similar.

The misfit curves from Figure 8, from which the models form the basis of the histograms in Figure 10, indicate that the MCMC method indeed retained only those models that fit the admittance within the given errors (as it should). While small parameter changes may change the fit for certain parameter combinations, those models with large misfits are not included in the MCMC results. Thus, the parameter distributions

presented in the histograms reflect the likely distributions in order to fit the admittance.

5.1.2. Varying the Degree Range

The only sensitivity that may be more difficult to capture is that with respect to the degree range used as explained above. Using a larger degree range should allow for a better determination of most of the parameters. We initially test this sensitivity for area 1, using the range 40–65. We chose this range because after this starting degree, the correlations have slightly dropped and start to rise again (see Figure 7), and this is more consistent with the correlation assumptions for the admittance model. Using this smaller range of degrees, the results for the parameters do not notably change when compared to the results using the larger degree range. We show the distributions using this narrower range in Figure A15 and the misfit to the admittance in Figure A16. The crustal density and load density become somewhat lower, and the elastic thickness increases, but all within the given spread. The load parameter does become larger, indicating more subsurface loading.

The robustness of the results for area 1 may also reflect the stable admittance curve in the degree ranges used; it is mostly flat, consistent with the theoretical models at higher degrees. Both degree ranges also capture the admittance inflection and should thus result in similar estimates of the parameters, as is indeed the case. For areas 1 and 2, we have the widest degree range, and our results may thus be the most robust for those areas.

For areas 3 and 4, we changed the localization to increase the range of degrees. We also performed the MCMC analysis for both areas using the originally selected localization parameters (a radius of 15° and $L_{\text{win}} = 22$). For area 3, this results in a degree range of 23–37, and for area 4, the range is 23–35.

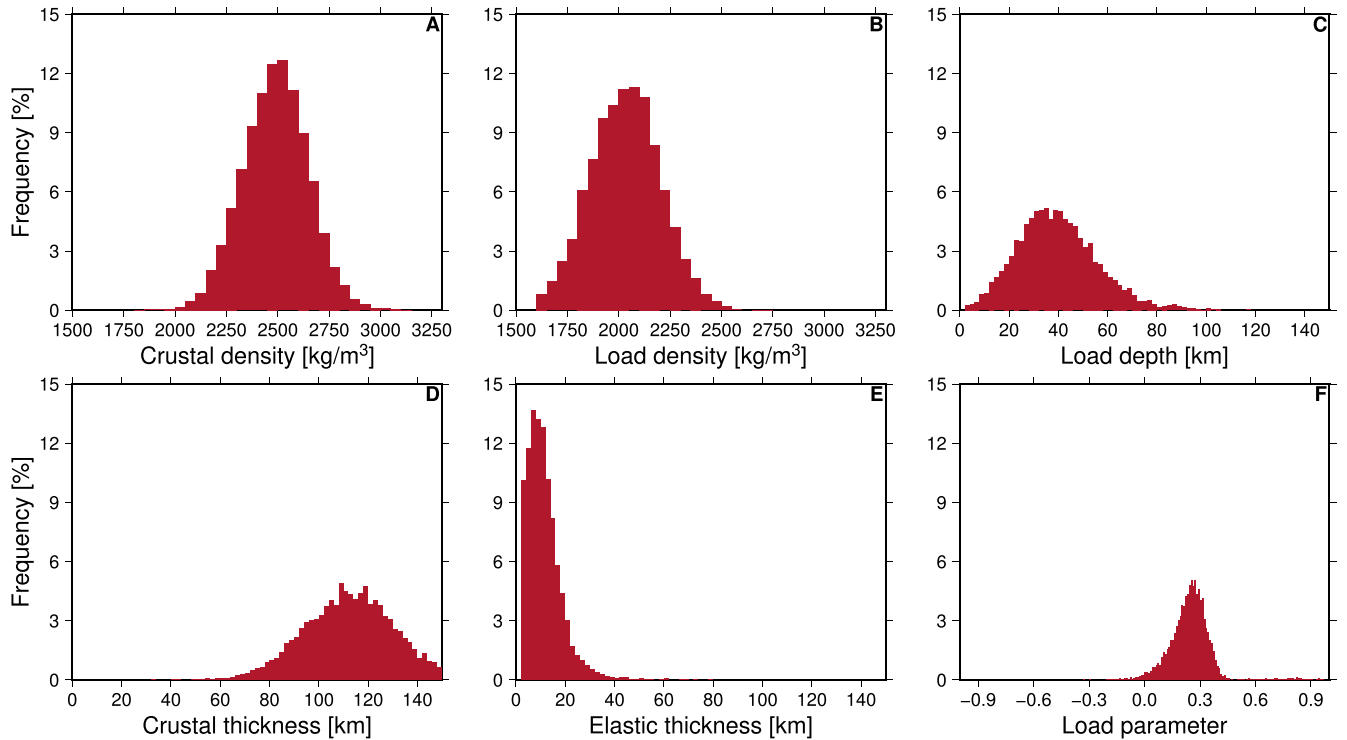


Figure 11. Results from the MCMC analysis for area 3, shown as a posteriori probability distributions for the estimated parameters: crustal density (A), load density (B), load depth (C), crustal thickness (D), elastic thickness (E), and load parameter (F).

Using these parameters, we can also fit the measured spectrum well for area 3 (see Figure A17A). We show the distributions for this case in Figure A18. The results for the densities and load parameters, however, are different from our nominal case presented in Section 4.3.3; the densities are higher for the case using $L_{\text{win}} = 22$, and the load parameter indicates strong subsurface loading, L being close to 1. The elastic thickness is larger for the case with $L_{\text{win}} = 22$.

With the originally selected localization, the admittance for area 4 does not include a downward trend, as can be seen in Figure A17B. We can again fit the admittance. The density results change with this localization. The load parameter is now clearly centered around zero. The lack of the downward admittance trend may mean that a nonzero load parameter is not necessary to fit the admittance. The load density is higher than the crustal density (which itself is relatively low), which also facilitates the top-loading scenario in this case. The crustal thickness is also larger when using $L_{\text{win}} = 22$.

5.1.3. Setting the Load Density Equal to the Crustal Density

For most of our areas under investigation (apart from area 4), the load might be more difficult to interpret, since we cannot localize on only one feature because of the resolution of the gravity field. The combination of load and crustal density may thus also indicate a more average crustal density. We tested this for area 1 by fixing the load density to be the same as the crustal density. For this case, the estimated density indeed becomes close to the average of the two, although the central value is slightly higher, at $2303 \pm 109 \text{ kg m}^{-3}$. The distributions for the other parameters are stable in this case (Figure A19), again showing the robustness of the MCMC results. The load parameter is now closer to zero as a result of forcing the densities to be equal.

5.1.4. Parameter Resolution

In several instances above, we indicated that we consider the elastic thickness and densities to be the most robustly determined parameters in our analysis. We investigated this in more detail in two ways. First, we conducted a simulation using the parameters of area 1, where we constructed “truth” admittance using a set of parameters and then applied MCMC to fit this admittance spectrum. We used the same errors on admittance in this simulation that we used in our actual analysis for this area. We then compared the ensemble average with the input parameters. We confirmed that the relatively large errors are due to the intrinsic nonuniqueness because we again find similar spreads when we use 1σ or 3σ errors. We also find that elastic thickness, load density, and crustal density appear to be the best-resolved parameters.

Second, we investigated the second derivative with respect to the parameters of the localized admittance function evaluated at the ensemble average state. This Hessian matrix can indicate whether we have found the minimum of the cost function, and it can inform us about the sensitivity of the system with respect to the parameters. We compute this Hessian matrix numerically using a finite difference method, obtaining a 6×6 matrix (there are six parameters). We then compute the eigenvalues and eigenvectors of this system. This shows that in general, two parameters are well resolved; for the two largest eigenvalues, the eigenvectors are very close to being unit vectors. In this analysis, these parameters are the load parameter and elastic thickness. The eigenvalues quickly decrease, and the eigenvectors indicate a less clear result for the other parameters. This is reasonably consistent with our interpretation and the simulation study. The most important result is that indeed, our elastic thickness results appear among the most robust.

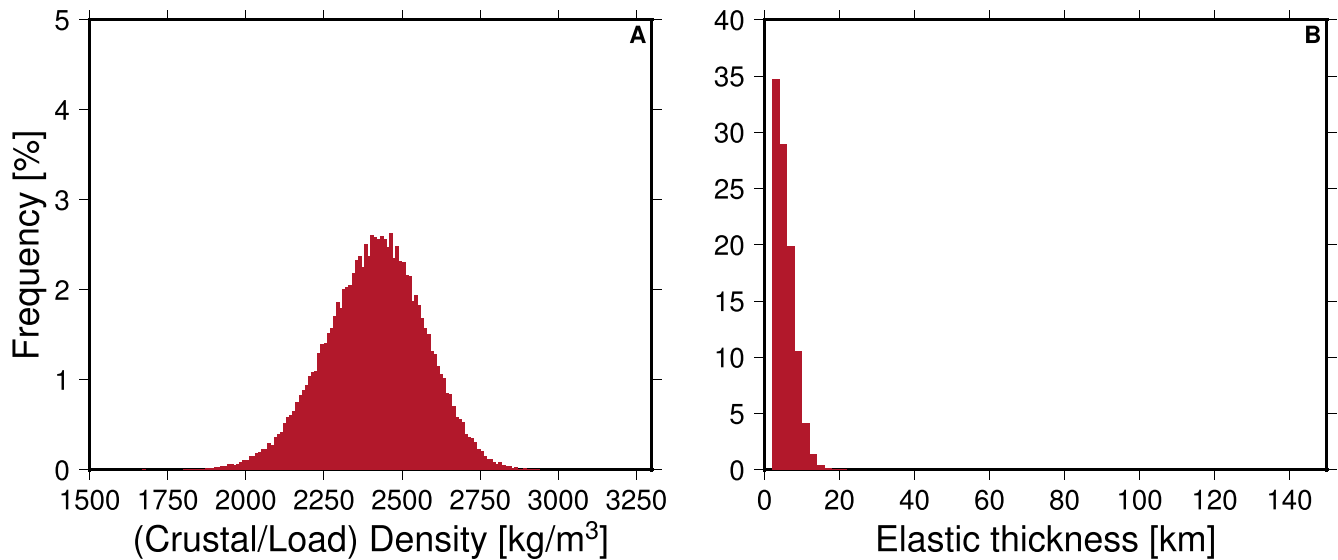


Figure 12. Results from the MCMC analysis for area 3, when we estimate only two parameters: density (A) and elastic thickness (B). We used the spectrum obtained with $L_{\text{win}} = 8$.

5.2. Northern Rise

For the northern rise, our results are consistent with earlier observations (e.g., James 2018), as stated in Section 4.3.4. A straightforward interpretation of the top-loading result would mean dense material covering the surface, yet as James (2018) stated, there is no obvious source for such a dense material, although intrusive volcanism in the top of the crust could possibly resolve this. We do not have depth constraints on a possible density contrast in the crust at the northern rise. Another possibility raised by James (2018) is that the cause of the northern rise lies deeper in Mercury, in the mantle or at the base of the crust. Recent analysis of magnetic data also hints at this (Plattner & Johnson 2021). In order to probe this, we reanalyzed the admittance curve for area 4, this time ensuring that the model has the load depth in the mantle ($z > T_c$), which also means a negative load parameter (Grott & Wic-zorek 2012). In this case, the distribution for several parameters changes (as shown in Figure A20). The crustal density becomes lower, with the load density not changing, which would still indicate the area as a high-density area. The load is located deep, as enforced in this case, and the load parameter is only slightly negative. While the results show no sensitivity to crustal thickness (there is a peak, but it is spread very widely), the distribution for elastic thickness is now also much wider, indicating no sensitivity to this parameter either.

Volcanism could have contributed to the high admittance values observed at the northern rise. Much of Mercury’s topography is a product of impact cratering, which is associated with high porosities (e.g., Christeson et al. 2018). In contrast, the porosity of a volcanic emplacement primarily results from vesicularity associated with volatile exsolution, which can be negligible (Vedanti et al. 2018). Furthermore, the heat of magmatic intrusions can trigger pore space closure in a previously porous crust (Wic-zorek et al. 2013). Relatively low porosity translates to relatively high bulk density, which produces high admittance values. Furthermore, intrusive volcanism could cause the near subsurface of the northern rise area to be more mafic (i.e., denser) than remote sensing indicates. An analysis focused on the northern rise with

specially constructed admittance models taking into account a larger degree range than here is thus warranted.

Interpretation for the northern rise remains difficult in these different scenarios, as both the nominal solution (where we enforce the load density to be larger than the crustal density, which results in a mostly top-loading scenario) and the solution with the load at depth seem plausible. The fit to the admittance for both is close (see Figure A21). A more detailed analysis of this area with a tailored admittance model that can include a wider range of degrees is warranted.

5.3. Elastic Thickness and Heat Flux

As indicated in Section 5.1.4, the elastic thickness appears well resolved in our analysis. Yet we also find surprisingly low values. The regions under consideration have modest levels of insolation (Williams et al. 2011), and this could mean that our values, already low, are slightly higher than the global average.

Elastic thickness can be related to heat flux. While a detailed analysis of elastic thickness and its meaning for the thermal state of the lithosphere is outside of the scope of this analysis, we can relate elastic thickness to heat flux in a first-order approach. Heat flux q can be expressed using Fourier’s law of heat conduction (e.g., Turcotte & Schubert 2002) and simplified by assuming a linear temperature gradient following

$$q = -k \frac{dT}{dr} = k \frac{T_{\text{base}} - T_{\text{surf}}}{T_e}, \quad (11)$$

where k is the coefficient of thermal conductivity, T is the temperature (at either the base of the lithosphere or the surface), and r is the radial coordinate. Low elastic thickness values such as we find for our four areas thus result in high heat flux values. If we assume the temperature at the base to be 1050 K (e.g., Breuer & Moore 2007) and use a surface temperature of 440 K (e.g., Padovan et al. 2014) and thermal conductivity of $3 \text{ W m}^{-1} \text{ K}^{-1}$ (e.g., Michel et al. 2013), then for $T_e = 20 \text{ km}$ (roughly the average of our range), $q = 105 \text{ mW m}^{-2}$, which is a very high heat flux. Assuming a low-conducting crust by a crustal conductivity of $2 \text{ W m}^{-1} \text{ K}^{-1}$ results in a surface heat flux of $q = 70 \text{ mW m}^{-2}$, which is still high.

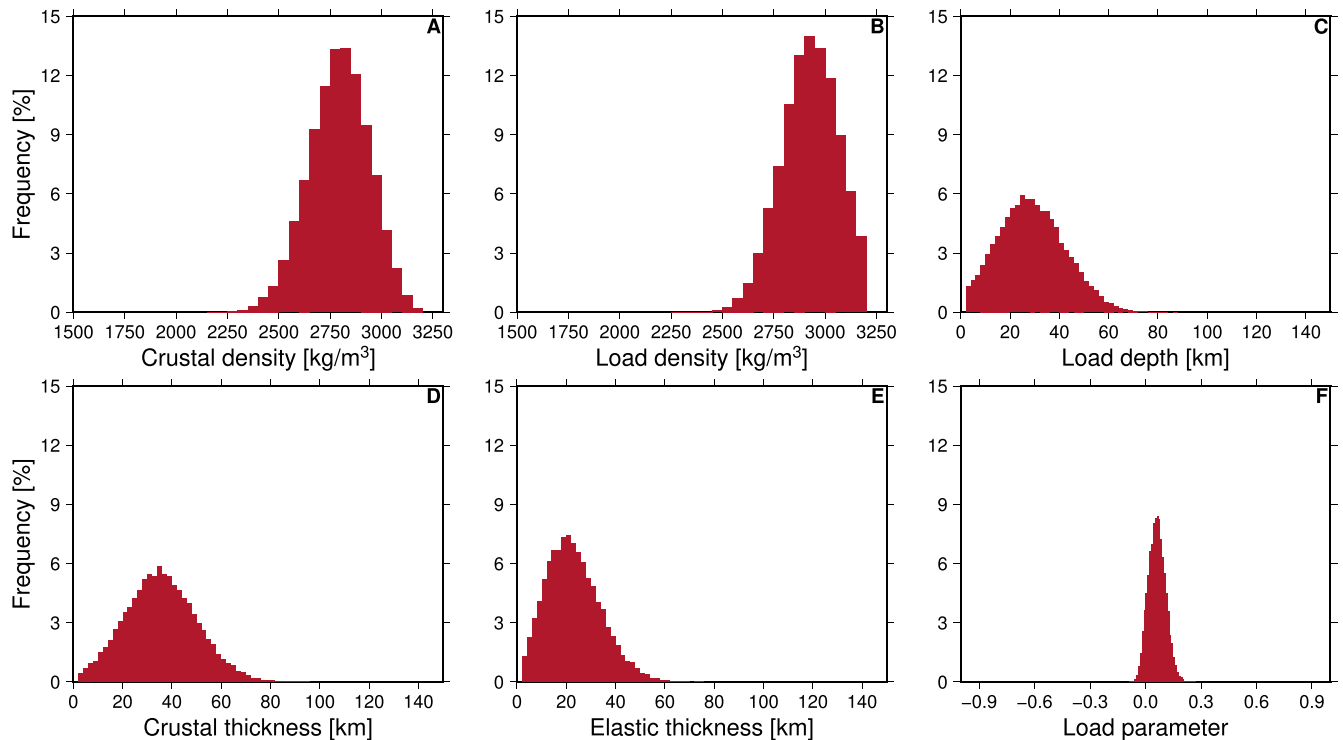


Figure 13. Results from the MCMC analysis for area 4, shown as a posteriori probability distributions for the estimated parameters: crustal density (A), load density (B), load depth (C), crustal thickness (D), elastic thickness (E), and load parameter (F).

Elastic thickness is related to a point in time when most of the topography was formed. For Mercury, most of the topography is either from impacts, which occurred mostly in the first billion years (e.g., Marchi et al. 2013), or from volcanism, which ended by about 3.5 Gya (e.g., Byrne et al. 2016). Hence, the elastic thickness values thus likely correspond to the early history of Mercury, 3.5–4.2 Gya. Our results for T_e and q thus indicate a high heat flux for early Mercury, at the time of formation of its topography (e.g., Ruiz et al. 2006). If the planet was (partially) molten at the end of accretion and cooled rapidly, a high initial heat flux is expected (Nimmo & Watters 2004). The latter found elastic thickness values of 25–30 km from a pre-MESSENGER analysis of faulting, while Watters et al. (2002) found a value of 40 km at 4 Gya. Both found lower heat fluxes in the range 10–50 mW m⁻². The upper ranges of our values for T_e are relatively consistent with those of Nimmo & Watters (2004).

5.4. Comparison for Crustal Density and Thickness

Our results can also be compared to earlier works. Elastic thickness was explored, for example, by Tosi et al. (2015). However, their focus was on the low-degree (degrees 2 and 4) geoid, resulting in planetwide high values for T_e , whereas ours focus on shorter wavelengths, and the results may thus not be readily comparable.

Crustal thickness was investigated in several studies (Padovan et al. 2015; Sori 2018; Beuthe et al. 2020a). Padovan et al. (2015) obtained a planetwide average of 35 ± 18 km from geoid-to-topography ratios. Sori (2018) argued for a thin, dense crust for Mercury, with an average crustal thickness of 26 ± 11 km. Our results, which are much more local than the two results mentioned here, contradict the latter, as we generally find lower densities and a thicker crust (see Table 3), except for the northern

rise. The difference in crustal thickness could be related to the difference in density or method, as our admittance fits rely on a different degree range, for example. The resolution of the used gravity field model may also play a part, as Padovan et al. (2015) and Sori (2018) used the older, lower-resolution HgM005 model, which lacked the last mission year with the low-altitude data.

We also compared our results with a recent study by Beuthe et al. (2020a). In contrast to the other studies mentioned here, they used the more recent gravity field model HgM008, and they explored various crustal density models; in addition to a crust of uniform density, they also considered models based on a crust with variable density. The variable crustal density model is based on surface mineralogy from geochemical mapping and laboratory experiments. A grain density map was derived for the surface, and the crustal density was derived assuming a surface porosity and a compaction model (increase of density with depth). Their crustal thickness based on a uniform crustal density is similar to the results presented in Genova et al. (2019), who presented the first crustal thickness model based on high-resolution gravity (assuming a uniform crustal density).

We list values for crustal density and thickness in Table 4. We obtained the crustal thickness and density models from Beuthe et al. (2020a) from their data archive (Beuthe et al. 2020b). For crustal thickness, we used their uniform density model, “U0”; their variable density models with 24% porosity, “V0”; and 12% porosity, “V1” because these are obvious end-members to test our results against. Because our crustal thickness values tend to be high, we also include their “thick crust” model “V4.” The V models have a high value for the correlation between crustal thickness and mantle melting, whereas the “U0” model does not. For the values for crustal thickness and density for each area from the models of Beuthe et al. (2020a), we took the average

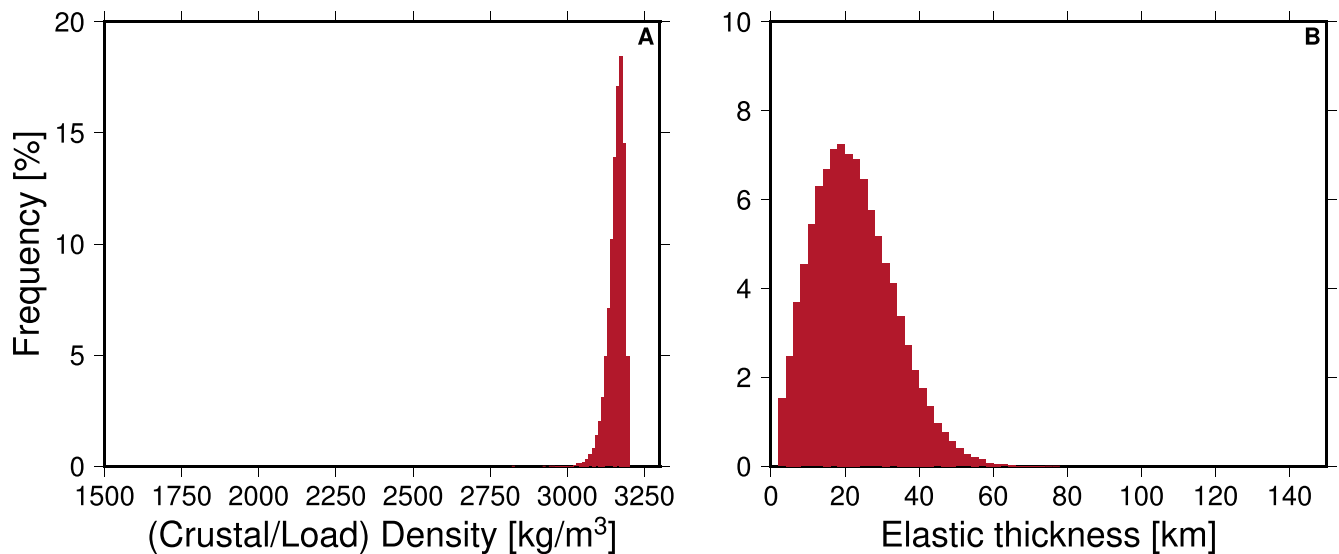


Figure 14. Results from the MCMC analysis for area 4, when we estimate only two parameters: density (A) and elastic thickness (B). We used the spectrum obtained with $L_{\text{win}} = 8$.

density in the spherical caps that we used for our localizations. Because Beuthe et al. (2020a) did not provide errors on their densities or thicknesses, we assign errors to each value in Table 4 by taking the standard deviation around the mean in the spherical cap. This is not an actual error and is thus likely to be an underestimate. We also note that their results depend on their assumption for the average thickness of Mercury’s crust. We find that for areas 1 and 2, our crustal thickness values correspond with those from Beuthe et al. (2020a) if we take the lower bounds; our central values are higher, and again, the spread in our values is also large. For area 3, our results indicate results that are very different: a much thicker crust, whereas Beuthe et al. (2020a) found a thinner crust. For the northern rise, however, we find a density that is relatively close to that of Beuthe et al. (2020a). Our results match even better for areas 1, 2, and 4, when we compare them to their “thick crust” model.

The densities we find are mostly consistent with the 12% porosity variable density values from Beuthe et al. (2020a), at least within our (relatively large) errors. The results for area 3 using the localization with $L_{\text{win}} = 22$ would indicate a higher density, whereas the crustal density for area 4 would be much lower for that same localization (but the load density is then close to what we find for the results using $L_{\text{win}} = 8$). When we estimate only two parameters, the densities for areas 3 and 4 increase and would be higher than those of Beuthe et al. (2020a). The densities we find for area 4 are close to the grain density reported by Beuthe et al. (2020a) and even higher than that, close to the mantle density, when we estimate only two parameters. For the other areas, if we assume the combination of load and crustal density to indicate an average crustal density, our results would be closer to the 24% porosity density values.

Our results indicate variations of the lithospheric properties for Mercury. With large error bars, the densities we find for three areas are fairly consistent and lower than perhaps generally assumed, in the range of 2500–2600 kg m⁻³, noting that, following the results from the Gravity Recovery and Interior Laboratory mission (Zuber et al. 2013), the Moon’s crustal density was found to be lower than assumed (Wieczorek et al. 2013). For area 4, the northern rise, our results may be

affected by the smaller degree range we used to fit the admittance, despite increasing the cap radius and decreasing the windowing bandwidth. This may result in less reliable results for parameters such as crustal density (and thickness), although elastic thickness can be determined, since it mostly controls the admittance signal at lower degrees. We do find consistently higher densities for the northern rise using different localizations and degree ranges when fitting the admittance.

6. Conclusions

We analyzed the entire set of MESSENGER tracking data to determine a high-resolution gravity field model based on line-of-sight acceleration data instead of Doppler tracking. We showed that these line-of-sight accelerations have a greater sensitivity to small-scale features than Doppler data, which makes them suitable for high-resolution gravity field determination. We presented models based on these accelerations, showing that they have fewer streaks from orbital tracks, and they can resolve circular features in the gravity field. In order to quantify the latter, an analysis of localized correlations between gravity and topography was performed, and it was shown that the line-of-sight models can indeed have improved correlations with topography, especially in areas where tracking data were collected when the spacecraft was at a low altitude above the surface.

We explored the influence of increasing the resolution of the gravity field model and the influence of constraints. The latter are necessary in order to stabilize the solutions due to spatial variations in data coverage that may not allow the same global high resolution everywhere. It was found that having a looser constraint (in other words, having less of an influence of the constraint on the solution) improves the correlations in certain regions and also influences the admittance (the transfer function between topography and gravity). The latter becomes flatter at higher degrees, which is more in line with expectations from theoretical models. The looser constraints also result in higher admittance values, which is consistent with other recent studies.

We used this line-of-sight model in a study of admittance. Four areas on Mercury were selected where the correlations

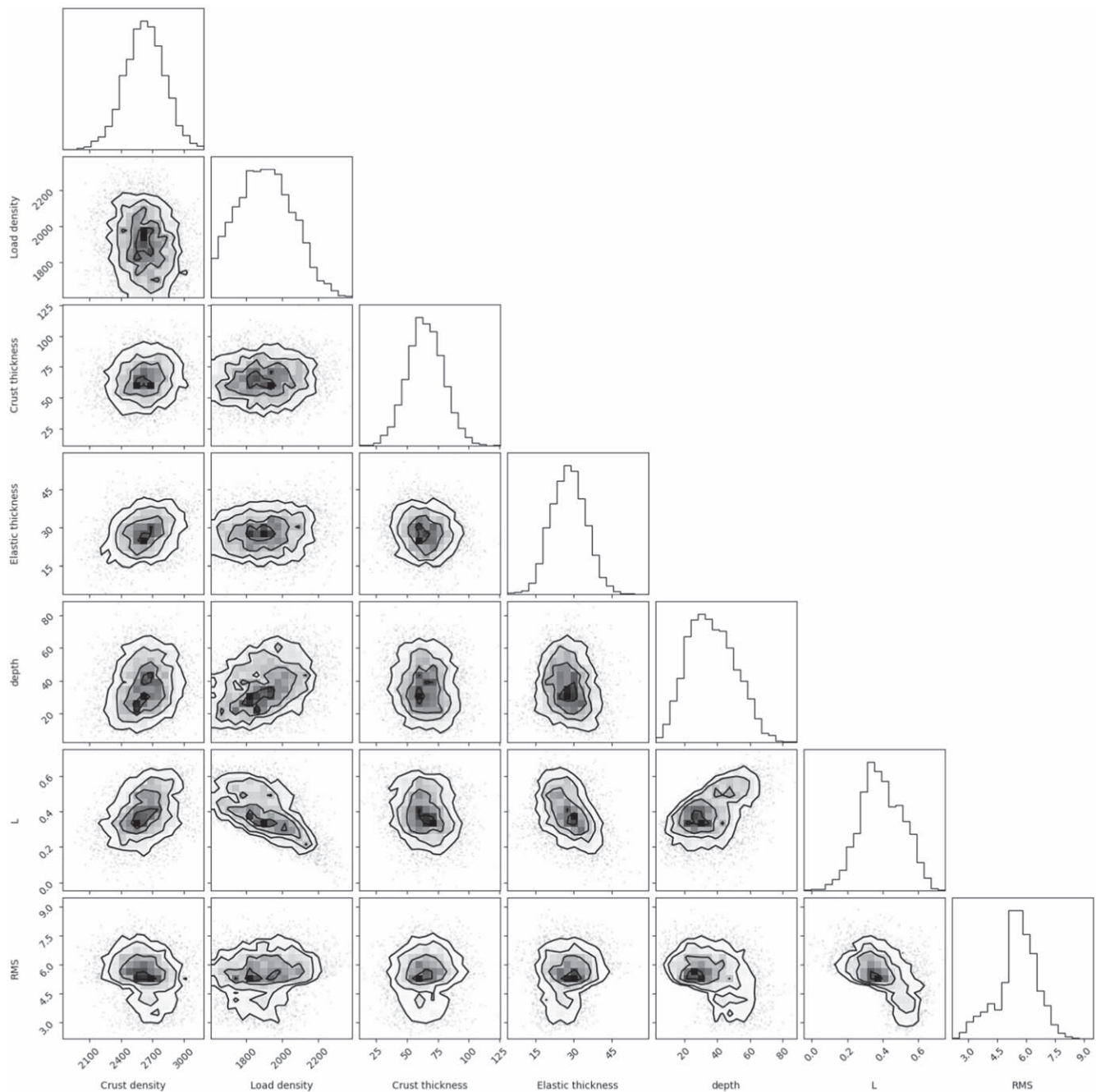


Figure 15. Results for area 1 from our MCMC analysis, where we plot the parameters against each other, including the rms of misfit for the admittance, in a triangle plot. This figure was made with the Python package “corner” (Foreman-Mackey 2016).

between gravity and topography were high enough to warrant such an analysis, because the assumption for this analysis is that gravity and topography correlate perfectly (a correlation value of 1). Two of the areas are in cratered terrains, one straddles an area with high topography, and the final area is centered on the northern rise, an area of high topography and gravity in Mercury’s northern smooth plains. We employ an admittance model originally developed for volcanic features on Mars. A Markov Chain Monte Carlo method was used to fit theoretical models of admittance to the measured, localized admittance spectrum. The estimation parameters are crustal density, load density, crustal thickness, elastic thickness, load depth, and a load parameter that describes the ratio between top and bottom loading.

The results indicate variations in the lithospheric properties at Mercury. For the cratered terrains and the area that straddles high topography, the density we find is between 2500 and 2600 kg m^{-3} , with lower load densities. If we assume the combination of load and crustal density to indicate the average crustal density in the area, the densities we find are close to 2300–2400 kg m^{-3} .

For the northern rise, we find a preference for a top-loading scenario, with a load density close to 3000 kg m^{-3} . The range of degrees used in the admittance analysis, however, is narrow (degrees 9–17), which may affect the estimates. When we limit our analysis to estimating only density and elastic thickness for the northern rise, we find an even higher density with a narrow distribution. Following recent results that indicate the northern

Table 4
Comparison of Crustal Thickness and Density Results with Beuthe et al. (2020a)

Parameter	Area 1	Area 2	Area 3	Area 4
	This Study			
Crustal density [kg m ⁻³]	2622 ± 190	2410 ± 205	2488 ± 160	2793 ± 146
	Results from Beuthe et al. (2020a)			
Grain density	3043 ± 84	2949 ± 47	2930 ± 32	2915 ± 46
Porosity 24%	2312 ± 64	2241 ± 36	2227 ± 24	2216 ± 35
Porosity 12%	2678 ± 74	2595 ± 41	2579 ± 28	2565 ± 41
	This Study			
Crustal thickness [km]	65 ± 15	53 ± 20	112 ± 17	36 ± 14
	Results from Beuthe et al. (2020a)			
Uniform density crust, model “U0”	29 ± 7	35 ± 5	35 ± 8	27 ± 4
Variable density crust (24% porosity, model “V0”)	44 ± 11	33 ± 6	31 ± 7	23 ± 6
Thick crust, model “V4” (24% porosity)	62 ± 18	42 ± 8	40 ± 7	31 ± 8

Note. Errors for the results by Beuthe et al. (2020a) are obtained from the standard deviation from the mean of the density or thickness in the spherical cap area used for localization. These errors are likely to be underestimates of the actual error.

rise may originate deeper in Mercury, we enforced the load to be at depth. For such a scenario, the crustal density decreases and the load density increases, still indicating that the northern rise is a high-density area. The results do not seem to clearly favor the top-loading scenario over the deeper load scenario.





We find relatively low effective elastic thicknesses for all areas, ranging between 11 and 30 km. These values correspond to regions with modest levels of insolation, which implies that these elastic thicknesses may even be slightly higher than the global average. We also find that elastic thickness is often well determined in our analysis, as shown by the relatively narrow parameter distributions. These relatively low elastic thickness estimates could indicate high heat flow at the time of the formation of Mercury’s topography, although we leave a rigorous inference of heat flux for future work.

We compared our crustal thickness and density values to recent studies and found that, except for the northern rise, the density results are mostly consistent with those from Beuthe et al. (2020a) for their models using a spatially variable crustal density. While there are some differences, for the first two areas, both the crustal density and thickness compare well, whereas only the densities compare well for the third area. For the fourth area, our crustal thickness is relatively close, but we find higher densities. This could be due to the degree range used in our admittance study. If we compare our crustal thickness to their “thick crust” values, our results for areas 1, 2, and 4 match even better. These comparison results strengthen our presumption that the results for the first two areas are the most robust from our analysis.

The data used in this analysis can be found at the MESSENGER archive on the PDS. In particular, radio tracking data can be found at https://pds-geosciences.wustl.edu/messenger/mess-v_h-rss-1-edr-rawdata-v1/messrs_0xxx/data/odf/. Gravity and topography models in spherical harmonics can be found at https://pds-geosciences.wustl.edu/messenger/mess-h-rss_mla-5-sdp-v1/messrs_1001/data/shadr/. The crustal thickness and density models from Beuthe et al. (2020a) were obtained from their data archive at Zenodo (Beuthe et al. 2020b), which can be found at <https://zenodo.org/record/3727115>. Results from this analysis are available at Zenodo: [10.5281/zenodo.6547874](https://zenodo.org/record/6547874), and at our data archive, <https://pgda.gsfc.nasa.gov/products/84>. At these links, we provide the Appendix,

gravity field models, and results of our MCMC analysis. We thank Terence Sabaka (GSFC) for discussions. We thank two anonymous reviewers for their constructive comments. This work was supported by NASA grant 80NSSC17K0218. All figures were generated with the freely available software GMT (Wessel et al. 2013). We used the freely available software SHTOOLS (Wieczorek et al. 2018) for all localizations. We are grateful for the support of the NASA Center for Climate Simulation (NCCS) at NASA Goddard Space Flight Center. We used their supercomputer facilities extensively for this work.

ORCID iDs

Sander Goossens  <https://orcid.org/0000-0002-7707-1128>
 Antonio Genova  <https://orcid.org/0000-0001-5584-492X>
 Peter B. James  <https://orcid.org/0000-0003-0350-1188>
 Erwan Mazarico  <https://orcid.org/0000-0003-3456-427X>

References

- Anderson, J. D., Schubert, G., Jacobson, R. A., et al. 2004, *Sci*, 305, 989
 Audet, P. 2014, *PEPI*, 226, 48
 Barriot, J.-P., & Balmino, G. 1992, *Icar*, 99, 202
 Barriot, J.-P., & Balmino, G. 1994, *Icar*, 112, 34
 Barriot, J.-P., Valès, N., Balmino, G., & Rosenblatt, P. 1998, *GeoRL*, 25, 3743
 Becker, K. J., Robinson, M. S., Becker, T. L., et al. 2016, *LPSC*, 47, 2959
 Beuthe, M., Charlier, B., Namur, O., Rivoldini, A., & Van Hoolst, T. 2020a, *GeoRL*, 47, e87261
 Beuthe, M., Charlier, B., Namur, O., Rivoldini, A., & Van Hoolst, T. 2020b, Mercury’s crustal thickness correlates with lateral variations in mantle melt production: Dataset for maps of surface density, degree of partial melting, and crustal thickness, Zenodo, doi:10.5281/zenodo.3727115
 Beuthe, M., Rosenblatt, P., Dehant, V., et al. 2006, *GeoRL*, 33, L03203
 Breuer, D., & Moore, W. B. 2007, in *Planets and Moons. Treatise on Geophysics*, ed. G. Schubert, Vol. 10 (Amsterdam: Elsevier), 299
 Broquet, A., & Wieczorek, M. A. 2019, *JGRE*, 124, 2054
 Byrne, P. K., Klimczak, C., Şengör, A. M. C., et al. 2014, *NatGe*, 7, 301
 Byrne, P. K., Ostrach, L. R., Fassett, C. I., et al. 2016, *GeoRL*, 43, 7408
 Cavanaugh, J. F., Smith, J. C., Sun, X., et al. 2007, *SSRv*, 131, 451
 Chapman, C. R. 1988, in *Mercury*, ed. F. Vilas, C. R. Chapman, & M. S. Matthews (Tucson, AZ: Univ. Arizona Press), 1
 Christeson, G. L., Gulick, S. P. S., Morgan, J. V., et al. 2018, *E&PSL*, 495, 1
 Crosby, A., & McKenzie, D. 2005, *Icar*, 173, 100
 Ermakov, A. I., Park, R. S., & Bills, B. G. 2018, *JGRE*, 123, 2038
 Foreman-Mackey, D. 2016, *JOSS*, 1, 24
 Genova, A., Goossens, S., Mazarico, E., et al. 2019, *GeoRL*, 46, 3625
 Genova, A., Mazarico, E., Goossens, S., et al. 2018, *NatCo*, 9, 289
 Goossens, S., Sabaka, T. J., Nicholas, J. B., et al. 2014, *GeoRL*, 41, 3367
 Grott, M., & Wieczorek, M. A. 2012, *Icar*, 221, 43

- Hastings, W. K. 1970, *Biometrika*, **57**, 97
- Hauck, S. A., Margot, J.-L., Solomon, S. C., et al. 2013, *JGRE*, **118**, 1204
- Heiskanen, W. A., & Moritz, H. 1984, *Physical Geodesy* (Graz, Austria: Inst. of Physical Geodesy)
- James, P. B., Zuber, M. T., Phillips, R. J., & Solomon, S. C. 2015, *JGRE*, **120**, 287
- James, P. B. 2018, LPI Contribution, **2047**, 6053
- Johnson, C. L., & Hauck, S. A. 2016, *JGRE*, **121**, 2349
- Kaula, W. M. 1966, *Theory of Satellite Geodesy, Applications of Satellites to Geodesy* (Waltham, MA: Blaisdell Publishing Company)
- Kaula, W. M. 1996, *JGR*, **101**, 4683
- Kay, J. P., & Dombard, A. J. 2019, *Icar*, **319**, 724
- Klimczak, C., Byrne, P. K., & Solomon, S. C. 2015, *E&PSL*, **416**, 82
- Konopliv, A. S., Asmar, S. W., Carranza, E., Sjogren, W. L., & Yuan, D. N. 2001, *Icar*, **150**, 1
- Konopliv, A. S., Banerdt, W. B., & Sjogren, W. L. 1999, *Icar*, **139**, 3
- Konopliv, A. S., Park, R. S., & Ermakov, A. I. 2020, *Icar*, **335**, 113386
- Kusche, J. 2003, *AdG*, **1**, 81
- Manthilake, G., Chantel, J., Monteux, J., et al. 2019, *JGRE*, **124**, 2359
- Marchi, S., Chapman, C. R., Fassett, C. I., et al. 2013, *Natur*, **499**, 59
- Mazarico, E., Genova, A., Goossens, S., et al. 2014, *JGRE*, **119**, 2417
- McKenzie, D., & Nimmo, F. 1997, *Icar*, **130**, 198
- Metropolis, N., Rosenbluth, A. W., Rosenbluth, M. N., Teller, A. H., & Teller, E. 1953, *JChPh*, **21**, 1087
- Michel, N. C., Hauck, S. A., Solomon, S. C., et al. 2013, *JGRE*, **118**, 1033
- Montenbruck, O., & Gill, E. 2000, *Satellite Orbits* (Berlin: Springer)
- Mosegaard, K., & Tarantola, A. 1995, *JGRB*, **100**, 12431
- Muller, P., & Sjogren, W. 1968, *Sci*, **161**, 680
- Neumann, G. A. 2016, http://pds-geosciences.wustl.edu/messenger/mess-h-rss_mla-5-sdp-v1/messrs_1001/data/shadr/gtmes_150v05_sha.tab
- Nimmo, F., & Watters, T. R. 2004, *GeoRL*, **31**, L02701
- Padovan, S., Margot, J.-L., Hauck, S. A., Moore, W. B., & Solomon, S. C. 2014, *JGRE*, **119**, 850
- Padovan, S., Wieczorek, M. A., Margot, J.-L., Tosi, N., & Solomon, S. C. 2015, *GeoRL*, **42**, 1029
- Palguta, J., Anderson, J. D., Schubert, G., & Moore, W. B. 2006, *Icar*, **180**, 428
- Pavlis, D. E., & Nicholas, J. B. 2017, *GEODYN Documentation*, Goddard Earth Science Projects, NASA, <https://earth.gsfc.nasa.gov/geo/data/geodyn-documentation>
- Plattner, A. M., & Johnson, C. L. 2021, *GeoRL*, **48**, e94695
- Preusker, F., Stark, A., Oberst, J., et al. 2018, LPI Contribution, **2047**, 6031
- Ruiz, J., Tejero, R., & McGovern, P. J. 2006, *Icar*, **180**, 308
- Simons, F. J., & Dahlen, F. A. 2007, *Proc. SPIE*, **6701**, 670117
- Smith, D. E., Zuber, M. T., Phillips, R. J., et al. 2012, *Sci*, **336**, 214
- Solomon, S. C. 1976, *Icar*, **28**, 509
- Solomon, S. C., McNutt, R. L., Gold, R. E., & Domingue, D. L. 2007, *SSRv*, **131**, 3
- Sori, M. M. 2018, *E&PSL*, **489**, 92
- Takahashi, F., Shimizu, H., & Tsunakawa, H. 2019, *NatCo*, **10**, 208
- Tapley, B., Schutz, B., & Born, G. 2004, *Statistical Orbit Determination* (Burlington, MA: Elsevier)
- Tosi, N., Grott, M., Plesa, A.-C., & Breuer, D. 2013, *JGRE*, **118**, 2474
- Tosi, N., Čadek, O., Běhounková, M., et al. 2015, *GeoRL*, **42**, 7327
- Turcotte, D., Willemann, R., Haxby, W., & Norberry, J. 1981, *JGR*, **86**, 3951
- Turcotte, D. L., & Schubert, G. 2002, *Geodynamics* (New York: Cambridge Univ. Press)
- Vedanti, N., Malkoti, A., Pandey, O. P., & Shrivastava, J. P. 2018, *PAPGe*, **175**, 2905
- Verma, A. K., & Margot, J.-L. 2016, *JGRE*, **121**, 1627
- Watters, T. R., Schultz, R. A., Robinson, M. S., & Cook, A. C. 2002, *GeoRL*, **29**, 1542
- Watters, T. R., Selvens, M. M., Banks, M. E., et al. 2015, *GeoRL*, **42**, 3755
- Weider, S. Z., Nittler, L. R., Starr, R. D., et al. 2015, *E&PSL*, **416**, 109
- Wessel, P., Smith, W. H. F., Scharroo, R., Luis, J., & Wobbe, F. 2013, *EOSTR*, **94**, 409
- Wieczorek, M. A. 2008, *Icar*, **196**, 506
- Wieczorek, M. A. 2015, in *Treatise on Geophysics*, ed. G. Schubert (2nd ed.; Oxford: Elsevier), 153
- Wieczorek, M. A., Meschede, M., Sales de Andrade, E., et al. 2018, *SHTOOLS: Version 4.3*, Zenodo, doi:10.5281/zenodo.1346663
- Wieczorek, M. A., Neumann, G. A., Nimmo, F., et al. 2013, *Sci*, **339**, 671
- Wieczorek, M. A., & Simons, F. J. 2005, *GeoJI*, **162**, 655
- Wieczorek, M. A., & Simons, F. J. 2007, *JFAA*, **13**, 665
- Williams, J.-P., Ruiz, J., Rosenburg, M. A., Aharonson, O., & Phillips, R. J. 2011, *JGRE*, **116**, E01008
- Wong, L., Buechler, G., Downs, W., et al. 1971, *JGR*, **76**, 6220
- Zuber, M. T., Smith, D. E., Phillips, R. J., et al. 2012, *Sci*, **336**, 217
- Zuber, M. T., Smith, D. E., Watkins, M. M., et al. 2013, *Sci*, **339**, 668